Towards the near-infrared detection of brown dwarf companions: Exploring methods to detect low mass stellar companions from blended spectra ⋆

J. J. Neal[1,2]† P. Figueira[3,1] N. C. Santos[1,2] C. Melo[3]

[1]*Instituto de Astrofísica e Ciências do Espaço, CAUP, Universidade do Porto, Rua das Estrelas, PT4150-762 Porto, Portugal*
[2]*Departamento de Física e Astronomia, Faculdade de Ciências, Universidade do Porto, Portugal*
[3]*European Southern Observatory, Alonso de Córdova 3107, Vitacura, Casilla 19001, Santiago 19, Chile*

ABSTRACT

In this paper we attempt to detect the near-infrared (nIR) spectrum of candidate brown dwarf (BD) companions around FGK stars in order to assert or discard their stellar nature. First, Individual nIR spectra are fitted to a synthetic binary model comprised of two PHOENIX-ACES spectra using a χ^2 approach. The observed spectra are wavelength calibrated and corrected for the atmospheric absorption with the aid of synthetic telluric models. This procedure was unable to successfully detect the spectra of the most massive companion in the sample. We explore how the companion recovery fitting performs on simulated observations and discuss reasons for the non-detection observed. From the injection-recovery analysis, this technique, in its current form, is insufficient to recover a companion below 3800 K, corresponds to an upper mass limit of around 600 M_{Jup}. A strong discrepancy between models and observations was found and is put forward as the main reason for the non-detection. This work highlights the challenges in the spectral detection of faint companions, and in particular the limitations of the companion detection with synthetic models at low companion/host flux ratios.

Key words: brown dwarfs – binaries: spectroscopic – infrared: stars – techniques: spectroscopic – methods: miscellaneous

1 INTRODUCTION

Brown dwarfs (BDs) are sub-stellar objects unable to achieve hydrogen fusion; with masses around $13 - 80\,M_{Jup}$ (Chabrier & Baraffe 2000) these objects bridge the gap between low-mass stars and giant planets. Without sustained fusion, brown-dwarfs cool down over time with an age-dependent cooling rate. Therefore, there is an inherent degeneracy between the mass, age and luminosity of a given BD(Burrows et al. 1997). The direct measurement of the mass of brown dwarf is the first step to break this degeneracy.

By observing BD in both radial velocity (RV) and astrometry, one can determine the objects' true masses. The RV technique provides a mass lower-limit ($M_2 \sin i$) of binary and planetary companions, while the complementary astrometry measurements can often provide mass upper-limits (e.g. Sahlmann et al. 2011). by observing with the two techniques simultaneously one can obtain a tridimensional characterization of the orbit.

Unfortunately, when compared to stellar or planetary companions, BD companions in short period orbits are very rare around Sun-like stars. Characterizing the few stars of this *brown dwarf desert* (Halbwachs et al. 2000; Zucker & Mazeh 2001; Sahlmann et al. 2011) and the establishment of benchmark BDs (e.g. Crepp et al. 2016) is crucial to constrain formation and evolution theories (Whitworth et al. 2007) and in understanding this sub-stellar population.

Recently, there has been a renewed interest in BD candidates triggered by exoplanetary searches. While several works found similar properties on the BD and exoplanet populations, like a similar mass density (Hatzes & Rauer 2015), others found intriguing differences, like the different host metallicity (Santos et al. 2017; Schlaufman 2018), a strong hint of different formation mechanisms.

Measuring or tightening the constraints of BD masses improves the understanding of mass dependence on BD formation processes. For instance, there is growing evidence that the larger giant planets and BD companions do not follow the well known metallicity-giant planet correlation seen in main-sequence stars with planets (e.g. Santos et al. 2004, 2017; Maldonado & Villaver 2017). Photometry along with stellar evolution models (e.g. Baraffe et al. 2003; Allard 2013) can also be used to estimate the mass of BD companions (e.g.

Moutou et al. 2017) if there is sufficient orbital separation, and a precise determination of the age (e.g. Soderblom 2010).

At the level of direct spectral analysis, one can attempt to recover the spectra of the BD companion through a differential analysis (Ferluga et al. 1997). Spectra collected at different orbital-phases are shifted to the rest frame of the host star and mutually subtracted to cancel out the spectrum of the host star, allowing the faint companion spectra to surface. Advances in high-resolution and near-infrared (nIR) capabilities should enable this technique to be applied to BDs and planet companions, in which smaller RV shifts can be resolved and the contrast ratio of the smaller companion is improved.

Observing in the nIR is specifically desirable for the cooler sub-stellar and giant planet companions as their thermal emission is stronger in the infrared when compared to the optical, improving the contrast ratio between the host star and companion. The high-resolution nIR spectrograph CRIRES, has allowed significant advances in recent years with the detection of atmospheric signatures like CO and H_2O, atmospheric winds and thermal profiles, rotation and orbital motion, for both transiting and non-transiting planets (e.g. Snellen et al. 2010, 2014; Brogi et al. 2012, 2014, 2016; Rodler et al. 2012; de Kok et al. 2013; Piskorz et al. 2016; Birkby et al. 2017).

The higher temperature and relatively larger size of BDs when compared to giant-planets makes the development of spectral recovery techniques for BD companions a logical step capable of providing input to formation models. The recent advent of many new high-resolution nIR spectrographs, such as, CARMENES (Quirrenbach et al. 2014), NIRPS (Bouchy et al. 2017) or SPIRou (Artigau et al. 2014), as well as, the CRIRES+ (Dorn et al. 2016) upgrade, motivate the study of nIR-oriented methodologies for spectral recovery.

It is important to note that the search and detection of faint secondary spectra is not only relevant to planetary atmospheres, and has been attempted previously for the stellar and substellar regime. Kolbl et al. (2015) developed a method to detect the presence of optical secondary spectra down to a flux ratio of 1 per cent in the hosts of *Kepler* transit candidates. The presence of which can cause ambiguities in the system configuration, and introduce important systematics of the measured planet radius. The characterization of the false positive probability rate for Kepler has been found to be as high as ~35 per cent Santerne et al. (2012),highlighting the strong incidence of the problem.

In this paper we aim at detecting spectroscopically the BD companions of FGK stars. In Sect. 2 we present the motivation for target selection, and in Sect. 3 we present the observations and reduction process, along with the spectral models used in this work. In Sect. 4 we explain our companion recovery technique and its applicability to these observations, while in Sect. 5 we apply companion recovery using a χ^2 approach. In Sect. 6 we discuss our results and in Sect. 7 we present our conclusions.

2   MOTIVATION AND TARGET SELECTION

Sahlmann et al. (2011) identified several candidate brown dwarf companions of FGK stars with $M_2 \sin i$ values >10 M_{Jup}., These objects were among the best characterized BD at the time of the observations, and we selected seven candidates visible in Period 89. The *K*-band was selected to achieve a high contrast of the BD relative to the host star, based on the extreme V-K colour indexes (>7.8) of the companions.

The target host stars are presented in Table 1 along with their stellar parameters, while the companion orbital parameters are provided in Table 2.

We note that some of these orbital parameters have been refined in the literature since the observations took place. The companion to HD 211847 was found to be a low mass star with an $M_2 = 155\, M_{Jup}$ (Moutou et al. 2017), while the companion to HD 4747 was found to have a mass of $M_2 = 60\, M_{Jup}$ (Crepp et al. 2016). The two companions of HD 202206 (B and c) were found to have masses of $M_B = 93.6\, M_{Jup}$ and $M_c = 17.9\, M_{Jup}$, respectively, classifying HD 202206c as a "circumbinary brown dwarf" (Benedict & Harrison 2017). These targets with recently refined masses create good benchmarks for us to compare any results of the techniques developed in this paper, and show that these masses do span the BD – low mass star range. All target companions except HD 162020 (P=8.4 days) are in (very) long period orbits (P=0.7–38 years) with masses (or $M \sin i$) greater than 10 M_{Jup}.

K-band spectra were obtained with the initial goal to achieve a direct detection of the companion spectra through the application of a spectral-differential approach (e.g. Ferluga et al. 1997; Kostogryz et al. 2013). Doing so would have enabled a further constraint to be placed on their masses. However the short time elapsed between observations and the long orbital periods led to an insufficient line separations to use a spectral-differential approach. This paper instead attempts to detect the companion spectra via fitting of these blended nIR spectra.

3   DATA AND DATA REDUCTION

3.1   CRIRES data

Observations were performed with the CRIRES instrument (Kaeufl et al. 2004) configured to observe a narrow wavelength domain of the *K*-band between 2120–2160 nm using the Ks and the Hx5e-2 filters. The slit width of 0.4 sec resulted in an instrumental resolving power of R = 50 000, with no adaptive optics to ensure that the slit was entirely covered by each target. This prevents strong slit illumination variations that could change the shape of spectral lines.

The observations were conducted in service mode during period 89 under run ID. 089.C-0977(A) between April and September 2012. An observation is composed of 8 individual spectra each with an integration time of 180 seconds, observed in a ABBAABBA nod cycle pattern to obtain a high (>180) signal-to-noise when combined.

The list of observations obtained with CRIRES are provided in Table 3. The SNR is calculated with the formula SNR $= \frac{\mu}{\sigma}$ where μ and σ are the mean and standard deviation in the continuum of detector 2 between 2130 and 2134 (see Fig. 2). The estimated RV values for the host and companion at the time of each observation are calculated using the radial velocity equations using the best known orbital parameters and the companion masses from Tables 1 and 2. For hosts with multiple companions the RV value is for the largest companion only, i.e. HD 202206B and HD 168443c. The RV difference between the host and the companion $rv_2 = (RV_2 - RV_1)$ is parameter used in the binary model from Sect. 4.3.2.

Table 1. Stellar parameters of the target companion's host stars. V is the apparent magnitude taken from SIMBAD (Wenger et al. 2000). Distances were calculated from the GAIA parallax measurements.

Star	SpT	V	$T_{\rm eff}$ (K)	logg (cm s^{-2})	[Fe/H]	M_1 ($M_\odot$)	Age (Gyr)	d (pc)	Reference
HD 4747	K0V	7.15	5316 ± 50	4.48 ± 0.10	−0.21 ± 0.05	0.81 ± 0.02	3.3 ± 2.3	18.80 ± 0.04	1, 2, 3, 8
HD 162020	K3V	9.12	4723 ± 71	4.31 ± 0.18	−0.10 ± 0.03	0.74 ± 0.07	3.1 ± 2.7	30.85 ± 0.06	4, 5, 6, 8
HD 167665	F9V	6.40	6224 ± 50	4.44 ± 0.10	0.05 ± 0.06	1.14 ± 0.03	0.7 − 3.6	31.24 ± 0.06	1, 8
HD 168443	G6V	6.92	5617 ± 35	4.22 ± 0.05	0.06 ± 0.05	1.01 ± 0.07	10.0 ± 0.3	39.67 ± 0.12	5, 6, 8
HD 202206	G6V	8.07	5757 ± 25	4.47 ± 0.03	0.29 ± 0.02	1.04 ± 0.07	2.9 ± 1.0	46.03 ± 0.14	5, 7, 8
HD 211847	G5V	8.62	5715 ± 24	4.49 ± 0.05	−0.08 ± 0.02	0.92 ± 0.07	0.1 − 6.0	48.81 ± 0.13	1, 2, 4, 8
HD 30501	K2V	7.59	5223 ± 50	4.56 ± 0.10	0.06 ± 0.06	0.81 ± 0.02	0.8 − 7.0	20.37 ± 0.01	1, 4, 8

References: (1) Sahlmann et al. (2011); (2) Santos et al. (2005); (3) Crepp et al. (2016); (4) Tsantaki et al. (2013); (5) Bonfanti et al. (2016); (6) Santos et al. (2004); (7) Sousa et al. (2008); (8) **?**;

Table 2. Orbital parameters for the BD companions obtained from the literature.

Object	γ (kms^{-1})	Period (day)	e	K_1 (ms^{-1})	T_0 (JD-2 450 000)	ω (deg)	$M_2 \sin i$ $M_{\rm Jup}$	M_2 $M_{\rm Jup}$	Ref.
HD 4747	0.215 ± 11	13826.2 ± 314.1	0.740 ± 0.002	755.3 ± 12	463.1 ± 7.3	269.1 ± 0.6	39.6	60.2	1
HD 162020	−27.328 ± 0.002	8.42819 ± 6e^{-5}	0.277 ± 0.002	1813 ± 4	1990.68 ± 0.01	28.4 ± 0.2	14.4	–	2
HD 167665	8.003 ± 0.008	4451.8 ± 27.6	0.340 ± 0.005	609.5 ± 3.3	6987.6 ± 29	−134.3 ± 0.9	50.3	–	3
HD 168443b	−0.047 ± 0.552	58.1124 ± 4e^{-4}	0.529 ± 0.001	475.13 ± 0.9	5626.20 ± 0.02	172.9 ± 0.1	7.7	–	4
HD 168443c	−0.047 ± 0.552	1749.83 ± 0.57	0.211 ± 0.002	297.7 ± 0.6	5521.3 ± 2.2	64.9 ± 0.5	17.1	–	4
HD 202206B	14.721	256.33 ± 0.02	0.432 ± 0.001	567 ± 1	2176.14 ± 0.12	161.9 ± 0.2	17.4	93.2 ± 7.3	5, 6
HD 202206c	14.721	1260 ± 11	0.22 ± 0.03	41 ± 1	3103 ± 452	280 ± 4	2.3	17.9 ± 2.9	5, 6
HD 211847	6.689^a	7929.4 ± 2500	0.685 ± 0.068	291.4 ± 12.2	12030.1 ± 2500	159.2 ± 2.0	19.2	155	3, 7
HD 30501	23.710 ± 0.028	2073.6 ± 3.0	0.741 ± 0.004	1703.1 ± 26.0	3851.5 ± 3.0	70.4 ± 0.7	62.3	89.6	3

^{a} fixed References: (1) Crepp et al. (2016); (2) Udry et al. (2002); (3) Sahlmann et al. (2011); (4) Pilyavsky et al. (2011); (5) Correia et al. (2005); (6) Benedict & Harrison (2017); (7) Moutou et al. (2017)

Table 3. Details about the each CRIRES observation. The time, settings, number of artefacts removed, the SNR obtained and the predicted orbital state of each system are provided.

Object	Obs. #	Start date (yyyy-mm-dd hh:mm:ss)	Filter	Airmass (at start)	Artefacts / 32	SNR	RV_1 kms^{-1}	RV_2 kms^{-1}	rv_2 kms^{-1}
HD 4747	1	2012-07-06 07:36:06	Ks	1.25	7	340	−0.219	−0.154	0.065
HD 162020	1	2012-07-04 06:23:22	Ks	1.30	2	127	−28.760	50.785^a	79.545^a
HD 162020	2	2012-07-04 06:57:48	Ks	1.44	2	128	−28.717	48.440^a	77.157^a
HD 167665	1	2012-07-28 05:00:53	Hx5e-2	1.24	7	371	7.581	18.024^a	10.443^a
HD 167665	2	2012-07-28 05:37:27	Hx5e-2	1.39	4	374	7.581	18.025^a	10.444^a
HD 167665	3	2012-08-05 02:54:03	Hx5e-2	1.04	4	358	7.575	18.163^a	10.588^a
HD 168443	1	2012-08-05 04:29:32	Ks	1.31	2	192	−0.121	50.932^{a,b}	51.053^{a,b}
HD 168443	2	2012-08-05 04:58:50	Ks	1.47	4	190	−0.121	51.189^{a,b}	51.310^{a,b}
HD 202206	1	2012-07-12 06:54:44	Ks	1.01	3	189	14.843	12.992^b	-1.851
HD 202206	2	2012-07-13 05:41:40	J	1.01	3	209	14.837	13.065^b	-1.772
HD 202206	3	2012-07-11 08:29:55	Ks	1.15	4	180	14.849	12.920^b	-1.929
HD 211847	1	2012-07-06 07:02:57	Ks	1.07	4	272	6.613	7.171	0.558
HD 211847	2	2012-07-13 06:54:37	Ks	1.05	5	283	6.614	7.167	0.553
HD 30501	1	2012-04-07 00:08:29	Hx5e-2	1.60	3	217	22.372	36.377	14.005
HD 30501	2	2012-08-01 09:17:30	Hx5e-2	1.42	10	212	22.505	35.120	12.615
HD 30501	3	2012-08-02 08:47:30	Hx5e-2	1.53	8	237	22.507	35.102	12.595
HD 30501	4	2012-08-06 09:42:07	Ks	1.28	7	235	22.514	35.031	12.517

^{a} Maximum RV given $M_2 \sin i$ only. ^{b} Largest mass companion only.

3.1.1 Data reduction

A custom IRAF[1] (Tody 1993) reduction pipeline (Figueira et al. 2010) was used to reduce the observations. It provides for auto-

mated dark and non-linearity corrections using the non-linearity coefficients provided by ESO, as well as the flagging and replacement of bad pixels. The images were corrected from sensitivity variations by dividing by the flat-field image corrected from the blaze function effect. The nodding pairs were mutually subtracted and the order tracing was fitted using either linear or cubic splines, selected for each detector.

Each spectra was extracted twice using the *rectangular* and

---

[1] IRAF is distributed by the National Optical Astronomy Observatories, which are operated by the Association of Universities for Research in Astronomy, Inc., under cooperative agreement with the National Science Foundation.
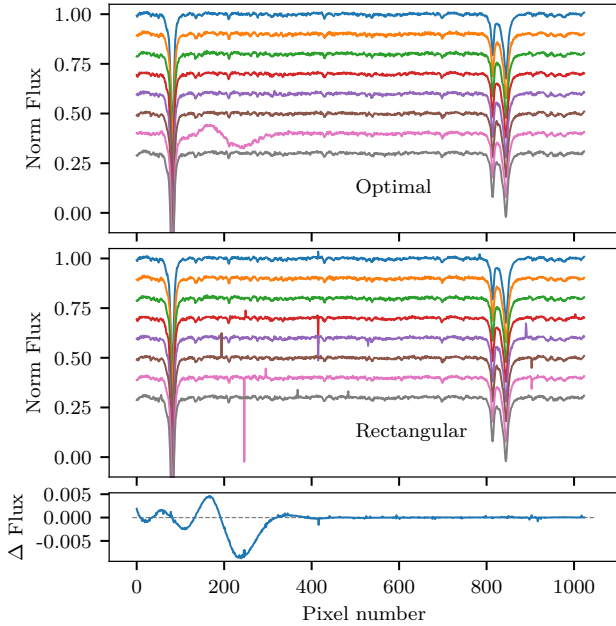
Figure 1. Example of an artefact in the optimally extracted spectra. The top panel contains the 8 normalized nod spectra after optimal extraction, while the middle panel shows the rectangular extraction for the exact same spectra. A vertical offset is included between each spectra. A single large spike in the seventh nod (pink) near pixel 230 creates a wide and noticeable artefact in the optimal extraction. The bottom panel shows the difference between a combined spectrum using the optimal nods only and a combined spectrum in which the seventh nod is replaced with its rectangular counterpart. The nod spectra are in observation order from top to bottom.

optimal extraction algorithms. The *rectangular* extraction performs a rectangular aperture sum in the spatial direction while the *optimal* extraction (Horne 1986) also includes variance weighting to reduce the impact of the noise and deviant pixels on the total flux measurement. The extracted nod-cycle spectra are continuum-normalized by division by a polynomial fit.

The average of the 8 nod-cycle spectra was used to create a combined spectra with a higher signal-to-noise. By default, the 8 optimally extracted spectra were used to create the combined spectra. However, on some observations spectral artefacts were visually identified in the *optimal* nod spectra. Several parameters of the reduction pipeline (e.g. the σ rejection limits and the aperture width) were adjusted in an attempt to remove these artefacts, but with limited success. To consistently remove these artefacts, in the affected exposures the nod spectra were replaced with their rectangular extraction equivalents. Since in a rectangular extraction the bad pixels are not flagged and removed, a iterative 4-σ rejection algorithm[2] was applied.

An example of a large extended artefact is given in Fig. 1. The top and middle panels show the the 8 normalized nod spectra for the *optimal* and *rectangular* methods respectively. In the top panel there is a clear deviation in the seventh nod spectra around pixel 200, which corresponds to a spike in the middle panel. The bottom panel shows the difference in the combined average spectra, between using only the optimal spectra and replacing those with artefacts,

in this case the seventh spectrum. These artefacts were observed to create flux deviations in the combined spectra up to ~0.5 per cent.

These artefacts had not been observed in previous works using this pipeline in the *H*-band, so this can be a wavelength-dependent affect. Alternatively, it can be an effect only affecting observations taken in some periods. The data gathered does not allow us to reach a conclusion.

The continuum normalization and nod combining steps were performed with IRAF while the following post reduction procedures and analysis utilize PYTHON. This pipeline was chosen over the ESO CRIRES pipeline because it was semi-automated, seemed relatively simple to use and, initial tests appeared to contain less bad pixel/cosmic ray artefacts in the extracted spectra compared to the ESO pipeline. In hindsight, the spectral artefacts observed decreased it's ease of use.

3.1.2 Wavelength calibration

Wavelength calibration of CRIRES data using Th-Ar hollow-cathode lamps is affected by important limitations (Kerber et al. 2009). The low density of Th-Ar lines in the nIR and the detectors narrow wavelength range (e.g. CRIRES-POP (Nicholls et al. 2017)) lead to a very low number of lines for defining a wavelength solution. Therefore, we use the telluric absorption lines present in each observed spectra as the wavelength reference. Instead of directly using the HITRAN database (Rothman et al. 2013) for the line positions of the telluric spectra (e.g. (Brogi et al. 2012, 2014; de Kok et al. 2013)), we use the TAPAS atmospheric transmission models (Bertaux et al. 2014) to simulate the telluric lines present on each observation. These in turn use the HITRAN database, but include atmospheric profiles and physical measurements to model the telluric absorption strength.

The centroid of each telluric line is obtained by fitting the telluric transmission spectrum, T, as a sum of Gaussian functions representing the individual telluric lines,

$$T(\lambda) = 1 - \Sigma_i \; G(\lambda, A_i, \mu_i, \sigma_i), \qquad (1)$$

where G is a Gaussian function of the form

$$G(\lambda, A, \mu, \sigma) = A e^{-(\lambda-\mu)^2/2\sigma^2} \qquad (2)$$

and A, μ, σ are the amplitude, central wavelength, and standard deviation for each line, respectively. Even though telluric lines are formally described by Voigt profiles, at 50 000 of resolution the lines are not fully resolved in the nIR and as such their shape is dominated by the convolution with the instrumental profile.[3].

The observed spectra contain thus two different components: the stellar and the telluric lines. Just like the telluric components, the stellar spectra can be well approximated by a sum of Gaussian Functions. The observed spectra correspond to the product of the stellar and telluric components. The identification of telluric and stellar lines is done assuming the synthetic telluric models are complete and allow to identify all the telluric lines. The spectra can then

---

[2] Found at https://github.com/jason-neal/nod_combination

[3] The instrumental profile for CRIRES has been shown to be well represented by a Gaussian shape (Seifahrt et al. 2010)

be represented mathematically by

$$I_{obs}(x) = I_{tell}(x) \times I_{star}(x)$$

$$I_{obs}(x) = \left(1 - \Sigma_j \, G(x, A_j, \mu_j, \sigma_j)\right) \times \left(1 - \Sigma_k \, G(x, A_k, \mu_k, \sigma_k)\right),$$
(3)

where x is the pixel coordinate of the extracted spectra.

The wavelength solution was obtained by fitting a second order polynomial, shown to be sufficient for higher precision RV studies (e.g. Bean et al. 2010; Figueira et al. 2010; Seifahrt et al. 2010), to the centroid values $\{\mu(x), \mu(\lambda)\}$ obtained from the telluric component of the observed spectra and telluric model, respectively.

Just like for the Th-Ar calibrations, this method only works when the available telluric lines cover the detector. For the wavelength setting of these observations, the spectra from the second detector (top right panel of Fig. 2) only have two large telluric lines present with several small lines, with relative depths smaller than 1 per cent, which are difficult to identify. This deteriorated the calibration stability for the second detector. While the lack of telluric contamination and stellar lines on the second detector makes it ideal for the detection of a faint secondary spectra it makes the process of wavelength calibration much more difficult.

We note that there are many variations on this wavelength-calibration technique, including those integrated within programs such as TelFit Gullikson et al. (2014), and ESOs Molecfit Smette et al. (2015), that perform telluric correction and re-calibrate the wavelength axis themselves. Including features such as concurrent fitting of a stellar spectral model, adjusted for RV, along with the telluric model, could help to improve the wavelength calibration performed here. For example Piskorz et al. (2016) while performing wavelength calibration using only a telluric line model on a wide range of wavelength, had to specifically include a stellar model around $2 \, \mu$m where the telluric lines are weaker.

3.1.3 *Telluric correction*

Ground based nIR observations require the removal of the absorption lines introduced by Earth's atmosphere. The observations analysed here were taken in an atmospheric window in the K-band in order to reduce the absorption introduced by the atmosphere (Barnes et al. 2008). To correct for the remaining telluric line contamination, the spectra were divided by the TAPAS(Bertaux et al. 2014) atmospheric transmission models computed for each observation. These synthetic telluric models were used to avoid the observing overhead necessary to perform telluric standard star exposures (Vacca et al. 2003), and they have been demonstrated to be superior in the quality of the correction relative to the telluric standard approach (e.g. Cotton et al. 2014).

The TAPAS (Transmissions of the AtmosPhere for AStronomical data) web-service[4] (Bertaux et al. 2014) was used to obtain atmospheric transmission models for each observation. TAPAS uses the standard line-by-line radiation transfer model code LBLRTM (Clough & Iacono 1995) along with the 2008 HITRAN spectroscopic database (Rothman et al. 2009) and Arletty atmospheric profiles derived using meteorological measurements from the ETHER data centre[5], which has a 6 hour resolution in atmospheric profiles. We use the mid-observation time to retrieve transmission models for each observation, with the Arletty atmospheric

profiles[6] and vacuum wavelengths. The telluric models were retrieved without any barycentric correction to keep the telluric lines at a RV of zero with respect to the instrument. We obtained one model with all provided species present, convolved to a resolution of R = 50 000, and another two models without an instrumental profile convolution applied. For these two extra models, one contained only the transmission spectra of H_2O while the other was for all other constituents except H_2O.

Before the correction, the depth of the telluric lines were rescaled to match the airmass of the observation using the relation T = T^β, where T is the telluric spectrum and β is the airmass ratio between the observation and model. This changed the depth of most absorption lines to match the observations, but does not correctly scale the deeper H_2O lines. The scaled telluric model is interpolated to the wavelengths of the observed spectrum and then used to correct the observed spectra.

We attempted the technique suggested by Bertaux et al. (2014) of fitting a scaling factor to the H_2O absorption lines before convolution to the instrument resolution as a way to address the poor H_2O airmass scaling. This was achieved by first dividing the spectrum by a telluric model with only non-H_2O constituents, convolved to the observed resolution, and scaled by the airmass to remove the non-H_2O lines. Then a model with only H_2O lines at full resolution was scaled by a factor T^x, convolved to R = 50 000 and compared to the observed spectra. The factor x was fitted to find the best scaling factor for the H_2O lines.

This method corrected the deeper telluric lines in a satisfactory way for some spectra in our sample, but in many cases we found that the fitted scaling factor was affected by the presence of blended stellar lines (attempting to fit those also) and dominated by the deepest H_2O telluric lines in the spectra analysed. We find that the telluric correction of the deep H_2O lines could be improved with this technique, but, at the cost of worsening the correction of the many smaller H_2O lines. Since the smaller H_2O lines covered a wider wavelength range of the spectrum than the larger lines we chose not to continue with this separate H_2O scaling. One possible solution for this would be to perform a piece-wise telluric correction, performing this step only for the deeper H_2O lines, or by using one of the other tools that fits the telluric model to the observations. This technique could also benefit from a larger wavelength span that would enable blended lines to be ignored while having sufficient deep H_2O lines to fit the scaling factor correctly. This small experiment shows that for cases like ours a simple scaling is not enough to correct for the absorption in an effective way.

After the telluric correction is performed, the spectra are corrected for Earth's barycentric RV using the helcor PyAstronomy[7] function ported from the reduce idl package (See Piskunov & Valenti (2002)).
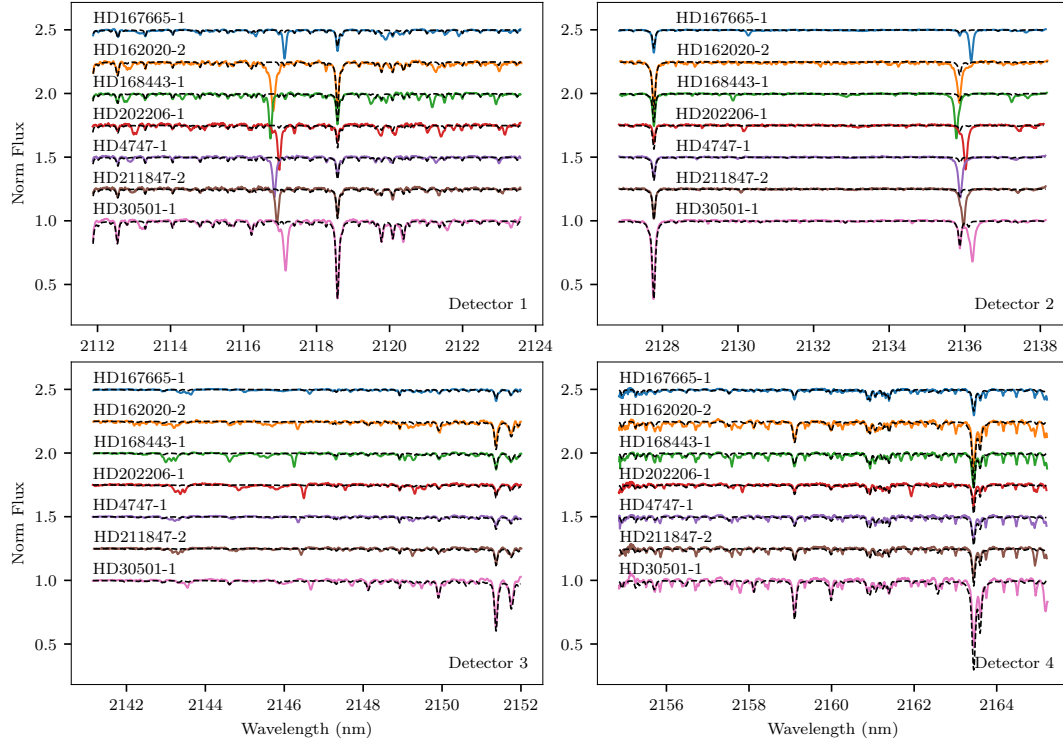
3.2 Wavelength masking

Poor wavelength calibration, the blending of stellar lines, and the imperfect telluric correction led to several wavelength regions being unusable to extract wavelength information, and these were masked in the subsequent analysis. Firstly, we removed regions near the edges of each detector where the wavelength solution is extrapolated outside the calibrating telluric lines region. This reduced the effective size of each detector by about 10 per cent or ~100 pixels.

---

[4] http://www.pole-ether.fr/tapas/
[5] http://www.pole-ether.fr

[6] Nearest of the 6 hourly profiles
[7] https://pyastronomy.readthedocs.io

Figure 2. Extracted, normalized and wavelength calibrated spectra for a single observation of each target. The target name is given above each spectrum along with the observation number. Each panel is the spectra from a single detector 1–4 in order of increasing wavelength. The black dashed lines indicate the unique telluric spectrum used for wavelength calibration and telluric correction for each observation.

Secondly, any remaining artefacts present and the centres of deep telluric lines where telluric correction was not corrected properly were masked out. These sometimes resulted in "emission-like" peaks in the corrected spectrum. These two factors led to masking out a further 10 per cent of the observed spectra.

As seen in Sect. 5 a further wavelength restriction leads to mask out regions where there is a large mismatch between the observed spectrum and the closest synthetic spectra for the host star. This significantly restricts the wavelength span utilized to around only 43 per cent. The masked regions are shown as the shaded areas in Fig. 6.

4   BINARY SYNTHETIC SPECTRAL RECOVERY

On the reduced, wavelength-calibrated and telluric-corrected spectra we attempt a spectral fitting of a binary model with the aim of detecting the presence of the faint spectra of the companion superimposed to that of the host star. The matching is done using χ^2 methods which have been extensively used in the literature (e.g. Astudillo-Defru et al. 2015; Passegger et al. 2016b; Zechmeister et al. 2018; Nemravová et al. 2016).

4.1   Synthetic PHOENIX-ACES models

The binary models were created using PHOENIX-ACES synthetic spectra library (Husser et al. 2013). It uses the most recent version (16) of the PHOENIX code and is suitable to reproduce the spectra of cool stars. The full parameter space of the PHOENIX-ACES spectra is given in Table 4, but we restrict our usage to the domain covered by the observation targets.

Table 4. Full parameter space of the PHOENIX-ACES spectral grid.

	Range	Step size
$T_{\rm eff}$ [K]	$2300 - 7000$	100
	$7000 - 12000$	200
logg	$0.0 - +6.0$	0.5
[Fe/H]	$-4.0 - -2.0$	1.0
	$-2.0 - +1.0$	0.5
α/Fe	$-0.2 - +1.2$	0.2

The spectral model libraries were accessed using the "grid tools" interface provided in the Starfish[8] python package (Czekala et al. 2015).

The synthetic spectra are multiplied by their wavelength to convert them into photon counts, ignoring multiplicative constants, as done in Figueira et al. (2016)[9]. The spectra are also convolved with a Gaussian kernel to match the resolution of the observations (R = 50 000). Due to the distributive property of convolution it is more efficient to apply convolution once to each synthetic spectra first, before the spectral pairs are combined.

The PHOENIX-ACES models include dust in equilibrium with the gas phase while ignoring dust opacity and not including any mixing/settling. They set a minimum library $T_{\rm eff} = 2300$ K to avoid the temperatures at which the modelling of clouds is necessary. This unfortunately limits the use of this library for this technique to the most massive mass companions in our sample. For example

---

[8] https://github.com/iancze/Starfish
[9] Synthetic models provide the spectral energy distribution (erg s^{-1} cm^2 cm^{-1}).

a T_{eff} = 2300 K corresponds to a BD with M ~ 84 M_{Jup} at 5 Gyr from the Baraffe et al. (2003) evolutionary models.

There are other spectral models that extend below 2300 K such as the BT-Settl models(Allard 2013; Baraffe et al. 2015). These are discussed in Sect. 6.1.6.

4.2 χ^2 method

The well known χ^2 technique measures the weighted sum of the squared deviation between the observation (O_i) and the computed models (C_i), with the minimum χ^2 value representing the best-fit parameters. The χ^2 is defined as

$$\chi^2 = \Sigma_i (O_i - C_i)^2 / \sigma_i^2, \tag{4}$$

where σ_i is the error on each measurement. We estimate the σ of each spectrum using the $\beta\sigma$ method (Czesla et al. 2018), using the MAD (median absolute deviation about the median) robust estimator. This method estimates the spectral noise using numerical derivatives of the spectra. We followed the procedure outlined in Czesla et al. (2018), analysing the results from successive parameter combinations to settle on an order of approximation (derivative level) of 5, and a jump parameter (pixels skipped to avoid correlations) of 2. We apply the same σ value to all points $\sigma_i = \sigma$. The $\beta\sigma$ method provided σ estimates for the target spectra which correspond inversely to signal-to-noise ratios between 100–500. These values are similar to the those given in Table 3 which were calculated from the continuum of detector 2 only.

The computed models are are interpolated to the wavelength grid of the observed spectra. The χ^2 is calculated by comparing the model and observation on their common wavelength grid. The results from all computed models is a multidimensional grid of χ^2 values for each combination of parameters, namely the spectral temperature, host RV, and companion RV for each detector, observation and target.

We obtain the global minimum of the multidimensional χ^2-space to represent the best fit to the observed spectra. We sum the multidimensional χ^2 across multiple detectors and determine a global minimum χ^2 for the whole observation $\chi^2_{obs} = \Sigma_{n=1}^{N} \chi_n^2$, where N is the number of detectors used. We do not, however, combine the χ^2 values across the separate observations as the RV parameters of the host and companion will vary between each observation.

The inverse survival function of the χ^2 distribution is used to determine the confidence levels on the minimum χ^2 parameters. The inverse survival function returns a $\Delta\chi^2$ value from the minimum χ^2 value for a given sigma level and degree of freedom. For example, the $\Delta\chi^2$ for a single degree of freedom required for the 1-, 2-, and 3-σ levels is 1, 4, and 9 respectively (Bevington & Robinson 2003). This method assumes that the measured flux is observed with a SNR sufficiently high so that the noise on the spectrum is approximately Gaussian, and as such the χ^2 method appropriate.

For a given observation, the χ^2_{red} is computed by $\chi^2_{red} = \chi^2/\nu$ where $\nu = n - m$, the number of observed pixels, n, minus the number of parameters of interest, m[10], and is performed after the summation over the detectors.

---

[10] m = 2 or 4 in the examples explored below

4.3 Computed model spectra

4.3.1 Single component model

The single component model C_i^1 is comprised of a single synthetic spectrum, J, (with model parameters T_{eff}, logg, [Fe/H], [α/Fe]), Doppler shifted by an RV of value rv_1.

It can be represented by the equation,

$$C_i^1(\lambda) = J(\lambda_0(1 - \frac{rv_1}{c})), \tag{5}$$

where λ is the shifted wavelength, λ_0, the model rest wavelength and, c, the speed of light in a vacuum. The model's flux is then continuum normalized to unity to match the observed spectra, and interpolated to the wavelength grid of the observation.

This single component model is similar to the χ^2 fitting performed by Passegger et al. (2016b). We apply the same renormalization (see Sect. 4.4) to account for slight differences in the continuum level and possible linear trends between the normalized observation and model. Unlike Passegger et al. (2016b) we do not apply any dynamical masking to sensitive lines to make the the χ^2 minima more distinct or linearly interpolate the stellar parameters between the grid models to obtain high precision stellar parameters. This is due to the differences in our end goals, detecting a secondary spectral component, compared to deriving precise stellar parameters. We also include radial velocity components to the χ^2 fitting, which is not included in Passegger et al. (2016b).

4.3.2 Binary model

We consider also the case of the superposition of two synthetic spectral components, for the host and the companion. Both spectra are Doppler shifted by rv_1, which represents the RV motion of the host star, while the companion spectra is also Doppler shifted by a second RV, rv_2, representing the RV offset between the host and companion. In this way the mean motion of the system relative to Earth is rv_1. The two spectra are scaled by their squared radius (see Sect. 4.3.3) and then added together, thus fixing their relative amplitude. Given two spectral components J_1 and J_2 with radii R_1, R_2 this translates to

$$C_i^2(\lambda) = J_1(\lambda_0(1 - \frac{rv_1}{c})) \times R_1^2 +$$
$$J_2(\lambda_0(1 - \frac{rv_1}{c})(1 - \frac{rv_2}{c})) \times R_2^2 \tag{6}$$

In the case of a BD companion around an FGK star investigated here, the continuum is dominated by the contribution from the host star as it contributes the majority of the spectrum with flux ratios below ~1 per cent for the 2110–2160 nm wavelength range. Since we are in the Rayleigh-Jeans regime for the star, that dominates the emission, the continuum of the combined spectrum is fitted and normalized using an exponential.

We combine the models in this way to represent the correct absolute flux ratio of the components. The median flux ratio between the two components is calculated for the wavelength range used here as an indication of the flux ratio level.

The full list of grid parameters for the binary model are $T_{eff}1$, $logg_1$, [Fe/H]$_1$, [α/Fe]$_1$, rv_1, $T_{eff}2$, $logg_2$, [Fe/H]$_2$, [α/Fe]$_2$, rv_2 where the subscripts 1 and 2 indicate the host and companion models respectively.

4.3.3 Effective radius

To combine the two synthetic spectra with the observed flux ratio we need to integrate the emitted flux over the effective surface area of each emitting body. Ignoring the common multiplicative constants that will disappear with normalization, we scale the two synthetic spectra individually by the square of their respective radii, R_1 and R_2.

In this work we use the effective radius (PHXREFF keyword) of each component from the PHOENIX model headers. This is the radius used in modelling of the stellar atmospheres. The ratio of the radii from the two synthetic spectra in the binary models are provided in Table 5.

We are aware that using these radii has its limitations, since as stated previously, there is a degeneracy in BD mass, age, and luminosity of the companion, and in particular a combination of radius-mass and radius-age relationships (Sorahana et al. 2013). Using the PHOENIX-ACES model effective radius does not allow for any independent age constraints to be incorporated, or allow for any variability in the radii to account for uncertainties.

The targets analysed here do not have transits, but if the radius ratio can be independently determined from the photometric transit method (Deeg 1998) then this could be used to constrain the radius ratio used when combing the binary model spectra instead.

4.4   Re-normalization

Remaining trends in the continuum level between the observed spectra and computed models were removed using the re-normalization following (Passegger et al. 2016b):

$$F_{re-norm}^{obs} = F^{obs} \cdot \frac{\text{continuum fit}_{model}}{\text{continuum fit}_{observations}}. \quad (7)$$

For detectors 1–3 a polynomial of first degree was used, while for detector 4 a quadratic function was used to fit the edge of a strong Hydrogen line (Brackett-γ) at 2166 nm, which lies just off of detector 4. This broad line is only observed in the synthetic spectra and not in the reduced observations. It is assumed that this was normalized out during the reduction process.

For each model we further allow the continuum level to be scaled with a factor between 0.95 and 1.05 and choose the model with the smallest χ^2 value.

4.5   Reducing the parameter space

The high dimensionality of the binary model makes it computationally challenging and difficult to analyse the χ^2 space. For reference, the multiplicative parameter space is squared when increasing from one spectral component in the single model to a binary model, and therefore becomes computationally expensive. In general the number of possible parameter combinations for c spectral components each with a grid of m models increases to c^m. If the full set of PHOENIX-ACES library spectra (66456) is explored with a binary fit then this naively balloons to over 4.4 billion possible combinations. Half of these are not unique as the host and companion components are swapped. This is the worst case scenario and we implement a number of assumptions to vastly reduce the parameter-space enabling faster computation.

Our first assumption is to restrict ourselves to models with an Alpha element abundance ([α/Fe]) of zero. This is in all likelihood a very good approximation as all our targets have solar metallicity and are thus very likely to belong to the thin disk of the Galaxy, where

[α/Fe] values are close to zero (i.e., solar) – e.g. Adibekyan et al. (2012). Our second step in simplifying the problem is assuming literature values for the host star metallicity and surface gravity given in Table 1. The metallicity of both components and the logg of the host star is fixed to the grid points closest to the literature values. The uncertainties on the literature measurements for metallicity (~0.05) and logg (~0.1) are both smaller than the grid steps of 0.5 used for these parameters. For the logg of the companion the Baraffe et al. (2003, 2015) evolutionary model value are used for the given companions $M_2/M_2 \sin i$ and hosts age.

We use the estimated companion temperatures from the Baraffe evolutionary models given the companion M_2 or $M_2 \sin i$ and stellar age as a starting point for the companion spectra grid computation and extend the grid in each direction, within the model limits. For example we show the companion temperature grid spanning −600 to +400 K in Fig. 3 and ±400 K in Figs. 4 and 5.

The large numbers stated above do not include the RV grid for each component. The number of spectra /models to consider increases when the RV grid step size is decreased (finer RV resolution). We can reduce the RV grid space significantly by tailoring it to the target being examined. For each target, we use the estimated RV values from the observation time and orbital parameters, given in Table 3 as a centre starting point for the rv_1 and rv_2 values and increment the RV within a few FWHM around those values, or out to the targets K_1 and estimated K_2 values.

An iterative process could be implemented to refine the RV grids, starting at a larger grid with lower RV resolution then performing a higher resolution grid about the minimum χ^2 RV values. This was only done manually but could have been automated. One could expect that a good starting RV grid step be governed by the spectral resolution, e.g. comparable to the FWHM velocity.

5   RESULTS

5.1   Simulated binaries

To test the companion recovery method we create simulated binary observations using PHOENIX-ACES spectra. White noise was added with a standard deviation $\sigma = 1/\text{SNR}$. We then applied the grid-matching recovery technique described above and compared the resulting parameters to the inputs.

The results of two example binary simulations are displayed in Figs. 3 and 4, both simulated with a SNR of 150. The input and recovered parameters for the binary components are indicated by the red circles and yellow stars, respectively, and are given in Table 5. The 3-σ contour indicates the shape of the confidence level. The 1-σ contours are not shown here as they are much smaller than the temperature grid step and are not easy to visualize. Each coloured rectangle is centred on the grid point, with its shape indicating the resolution of the grid space searched.

The first simulation shown in Fig. 3 is for a Sun-like star with a M-dwarf companion with a $T_{\text{eff}_2} = 4000$ K. The top-left panel shows the recovered host parameters when the single model is applied to the simulated binary. The top-right and both bottom panels are the parameters recovered when using the binary model. Both left-hand panels display the parameters for the host component to easily compare between models. With both models the host temperature T_{eff_1} is correctly recovered. The host RV, rv_1, is 0.1 km s^{-1} (two grid spaces) different from the simulated value for the single component model and is correctly recovered with the binary model.

The minimum χ^2 location for the companion temperature is

Table 5. Input and recovered parameters on simulations and an observation when applying a single (C^1) and binary (C^2) models. The logg and metallicity were fixed at $\mathrm{logg}_1 = 4.50$, $\mathrm{logg}_2 = 5.0$ and [Fe/H]=0.0 equally for both components. Gaussian noise was added to both simulations with a SNR of 150. Here m and n are the number of data points and parameters used in each model.

| | Simulation 1 | | | Simulation 2 | | | Observed HD 211847 | | |
| | Input | Recovered | | Input | Recovered | | Expected | Recovered | |
		C^1	C^2		C^1	C^2		C^1	C^2
T_{eff_1}	5800	5800	5800	5700	5800	5700	5715 ± 24	5900	5800
T_{eff_2}	4000	–	3800	3200	–	3100	~3200	–	>3800[a]
rv_1	0	0.1	0	6.6	6.6	6.6	6.6 ± 0.3	7	7.6
rv_2	10	–	9.8	0.5	–	-1	0.5 ± 2	–	-12.6
R_1/R_2	2.57	–	2.71	3.16	-	3.27	3.16	–	<2.71[a]
F_2/F_1	0.084	–	0.066	0.030	–	0.026	0.030	–	>0.066[a]
m	-	3072	3072	–	3072	3072	–	2612	2612
n	-	2	4	–	2	4	–	2	4
χ^2	–	4978	3792	–	3746	3630	–	37688	33860
χ^2_{red}	–	1.62	1.24	–	1.22	1.18	–	21.3	19.2
BIC	–	-20145	-22315	–	-21477	-21377	–	18281	14468

[a] At the arbitrary upper limit for companion temperature grid (3800 K).
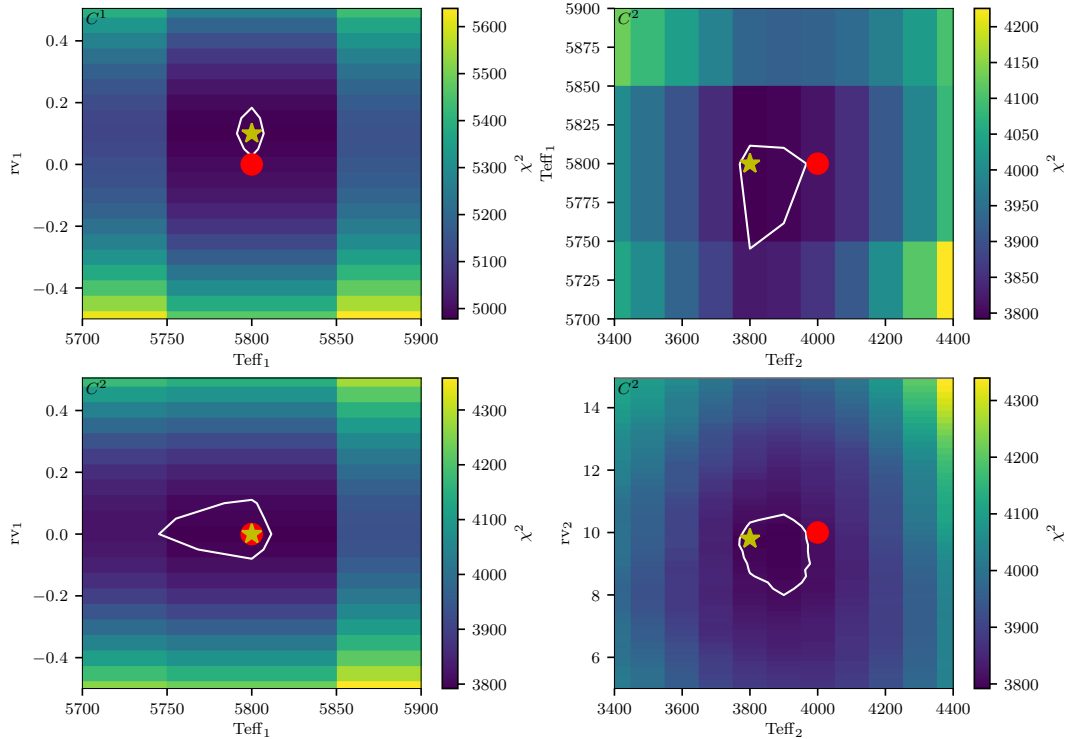
Figure 3. χ^2 results for companion recovery of a simulated binary observation of a Sun-like star (T_{eff_1} = 5800 K) with an M-dwarf companion (T_{eff_2} = 4000 K). The top right plot shows the application of a single component model (C^1) while the other three are using a binary model (C^2). Both left hand panels show the distribution of host temperature and host RV. The top right panel shows the distribution for host and companion temperature, and the bottom right the companion temperature and radial velocity. The red circle and yellow star indicate the location of the simulation input and recovered parameters respectively. The white line shows a 3-σ confidence level about the minimum χ^2 solution grid point. Each box is centred on the parameter values and shows the grid resolution.

200 K below the simulated value, and the RV of the companion recovered is $0.2\,\mathrm{km s^{-1}}$ below the input value. The input values for the companion are just outside of the 3-σ contours shown. The flux ratio for the input is 0.08 while the flux ratio recovered is 0.066.

The second simulation shown in Fig. 4 is performed with parameters to mimic the observation of our target with highest flux ratio, HD 211847. In this simulation the single component model

recovers a host with the correct RV but a temperature 100 K higher than the input value. Again, adding the companion with the binary model recovers the correct host temperature. The companion temperature recovered is 100 K lower than the input temperature and the RV is different by $2\,\mathrm{km s^{-1}}$ which is around one third the FWHM.

In this case with a companion RV offset, rv_2, near $0\,\mathrm{km s^{-1}}$ the host and companion lines are blended. The same spectral lines
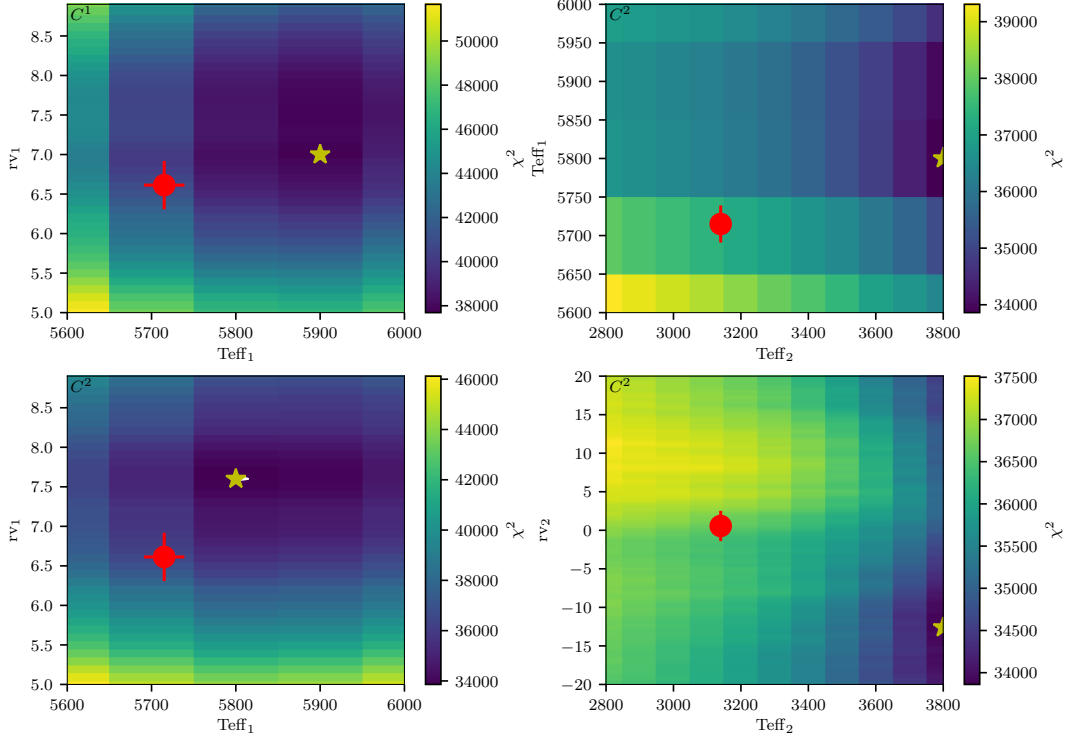
Figure 4. Similar to Fig. 3, χ^2 results for companion recovery of a simulated binary observation similar to HD 211847, (T_{eff_1} = 5800 K, T_{eff_2} = 3200 K). The top right plot shows the application of a single component model (C^1) while the other three are using a binary model (C^2). Both left hand panels show the distribution of host temperature and host RV. The top right panel shows the distribution for host and companion temperature, and the bottom right the companion temperature and radial velocity. The red circle and yellow star indicate the location of the simulation input and recovered parameters respectively. The white line shows a 3-σ confidence level about the minimum χ^2 solution grid point. Each box is centred on the parameter values and shows the grid resolution.

from both components are trying to match to the same features of the spectra, making it more difficult to recover the companion parameters. In the bottom right panel there appears to be multiple minima for different rv_2 and T_{eff_2} combinations, which we assume is partially due to the small rv_2.

In both simulations the reduced χ^2_{red} for the binary model is closer to 1. This is not surprising as the binary model contains additional parameters; extra components from the binary can fit components of the noise when a binary is not present, when has a low flux ratio, as is our case. We analyze the significance between the two models using the "Bayesian Information Criterion"(BIC) (Schwarz 1978);

$$BIC = n \ln (m) - 2 \ln (\hat{L}). \tag{8}$$

Here n and m are the number of parameters and data points respectively and $\hat{L}$ is the maximum of the Gaussian likelihood function

$$\hat{L} = \left(\frac{1}{\sigma \sqrt{2\pi}} \right)^m \exp \left(-\frac{\chi^2}{2} \right), \tag{9}$$

written in terms of χ^2 and a fixed σ for all data points. The maximum likelihood of a Gaussian distribution is equivalent to minimizing the χ^2. In both simulations $\Delta BIC > 10$ so the preference of the binary model, with the lower BIC value, over the single component model is considered *significant*.

5.2 HD211847 observation

HD 211847 is the best system in our sample to attempt a detection.

Even though it is not a BD binary system, the estimated flux ratio of 0.03 based on the Baraffe et al. (2015) evolution models and the known companion mass 155 M_J Moutou et al. (2017) make it the best target to test our detection capability. The result of applying χ^2 fitting to the second observation of HD 211847 is shown in Fig. 5.

For this target the metallicity of both components was fixed to 0.0 and the logg for the host was fixed at 4.5. The logg for the companion is fixed to 5.0, based on the Baraffe et al. (2015) evolutionary models for the given companion mass and system age. The orbital solution was used to refine the RV search space of both components. The span RV for the companion was extended until a value inside the RV bounds was found.

The top left panel of Fig. 5 shows the recovery with a single component model, with the other three for the binary model. The single component model finds a temperature of 5900 K for the host with a rv_1 of 7 km s^{-1}. This corresponds to an overestimation of 200 K and 0.4 km s^{-1} relative to the expected parameters. The binary model finds a host temperature of 5800 K, which is the second closest model to the literature value, >100 K different. The host RV value recovered with the binary model is 7.6 km s^{-1}, which is 1 km s^{-1} higher than expected. For the single component model there is a barely noticeable secondary minima near this 7.6 km s^{-1} RV value recovered by the binary model. Again these RV differences are smaller than the FWHM of the lines. The 3-σ contour is small, just visible on the right hand side of the star in the bottom left panel, and hidden behind the markers in the other panels.

For the companion in the binary model, on the right side of Fig. 5, the minimum χ^2 for the companion temperature is at the

upper temperature limit of the grid shown. If we extend the grid of companion temperature towards higher temperatures the best fit location continues to increase in temperature, continually hitting the upper limit until it is close to the host temperature, >2000 K above the expected companion temperature. When the companion temperature becomes this high it also affects the recovered parameters for the host star to offset the features of the brighter companion.

The χ^2_{red} values for the single and binary models are 21 and 19 respectively, far from 1, indicating that both models are a poor fit to the observations. The $\Delta BIC = 3812 > 10$ indicates that binary model is still preferred. We plot the binary model for the best fit solution alongside the observed spectra in Fig. 6. The low χ^2 show that none of the models is a good representation of the data; there is a large spectral mismatch between the synthetic models and the observation. Extra wavelength masking was applied to the largest mismatched synthetic lines to remove their influence. The grey areas mark regions which have been masked out, either from the centres of deep telluric lines (the thin masks matching spectral gaps), or the more prominent mismatched lines in the synthetic spectrum excluded from the χ^2 analysis. One clear example of a mismatched line is a synthetic line at 2132.5 nm that is clearly not observed in detector 2 (top right). Even with the majority of the mismatched lines removed the detection of the companion was still unsuccessful.

For detectors 1 and 2, it appears that the synthetic spectra contains many more deeper lines than observed. For detector 3 the red half of the detector was masked out as there appears to be an offset between the observed lines. With 3–4 lines that appear to be consistently offset from the observation it could be a wavelength calibration issue, although the telluric lines appear to be sufficiently corrected in this region, attesting for the quality of the wavelength calibration, and making it incompatible with the offset. For detector 4 the observed lines do not agree at all with the models. With many observed lines not in the model and only one line with some agreement in wavelength, detector 4 is masked out completely and not used in the χ^2 fit. Individual inspection of the χ^2 results for each detector also revealed that there was a large discrepancy between the 4th detector and the other three, with a different RV value for the host star and a χ^2 values an order of magnitude higher. The edge of a deep Hydrogen line (Brackett-γ) off the edge of the detector 4 is also clearly seen in the continuum of the model >2162 nm.

We applied this same method to the remaining targets, with similar results. In summary, we conclude that the companion spectra cannot be correctly detected in our data using this method.

5.3 Companion injection-recovery

To determine the detection limits for this method we employ an injection-recovery approach. We take the observed spectra and inject onto them a synthetic companion, at the absolute flux ratio to which it would have been added to a synthetic host with the same parameters. The injected companion RV is set to $100 \, \mathrm{km \, s^{-1}}$ so that the companion lines are well separated from the lines of the host. This separation chosen is only slightly larger than what we have with our observations, rv_2 given in Table 3.

We restrict the search space by fixing the host parameters T_{eff_1} and logg_1 to those recovered fitting the non-injected spectra by a single component model. The wavelength masking is used to reduce the level of mismatch between synthetic and observed spectra.

We apply the recovery method developed above on the injected spectrum, leaving only the companion T_{eff_2} and rv_2 parameters free, to recover the injected companion. We repeated this for injected companions with temperatures below 5000 K.

Table 6. Upper mass limits of target companions assuming a companion logg = 5.0. Masses are derived from Baraffe et al. (2015) evolutionary models using T_{eff} and logg. The flux ratio F_2/F_1 is the absolute flux ratio between the cut-off temperature and the target host star.

Target	T_{eff} cut-off (K)	F_2/F_1	Mass limit (M_{jup})
HD 4747	3900	0.084	598
HD 162020	3900	0.147	598
HD 167665	3800	0.054	560
HD 168443	4000	0.094	618
HD 202206	3900	0.075	598
HD 211847	3900	0.079	598
HD 30501	3800[a]	0.106	560

[a] From observed spectra

We also perform the injection-recovery with synthetic host spectra, representing each target. The wavelength range of the synthetic spectra used for this is three sections interpolated to 1024 values in the wavelength span of detectors 1, 2, and 3. For each section, Gaussian noise is added at the level measured in the corresponding detector for the in the observation of the target being represented.

In Fig. 7 we show the results of the injection-recovery on HD 30501. The blue dots represent the recovered companion temperature when injected into real observations, while the orange triangles represent injection into a synthetic host. Error bars of ± 100 K are included to indicate the grid size, and do not come from the recovery itself. The black dashed diagonal is the temperature 1:1 relation, where a correctly recovered companion should lie.

The grey shaded region indicates the ± 1000 K temperature range explored for the injection-recovery of the companion. This shows how the bounds of the grid are recovered at low temperatures.

For HD 30501 the injection onto synthetic and observed spectra produce similar results. At temperatures above 3800 K in both the real and synthetic the injected companion is recovered within 100 K. For injected companion temperatures below 3800 K the temperature recovered is systematically higher than the injected value. This indicates that the companion is not correctly recovered and is affected by the added noise. We determine this temperature to be the upper temperature limit for the recovery. For the other stars we could not conclude on the upper limit due to spectral mismatch issues. In these cases we use the results from the synthetic injection to derive a temperature recovery cut-off for each target, each simulated with the closest host star spectrum.

In Fig. 8 we show the minimum χ^2 for each companion temperature in the recovery grid. We do this for 7 different injected companion temperatures between 2500 and 4500 K. For the higher temperature companions, the χ^2 is parabolic in shape, recovering the correct temperature, as expected. At lower temperatures there is a strong asymmetry in the χ^2 with it flattening out on the lower temperature side. The 1-, 2-, 3-σ values (with 2 degrees of freedom) of 2, 6 and 11 above the minimum χ^2 are not shown in the bottom panel of Fig. 8 which is a close-up around the minimum χ^2 as are indistinguishable in the top panel due to the χ^2 y-scale. The black vertical line indicates the 2300 K temperature limit of the PHOENIX-ACES models.

Using the temperature cut-off values, we derive an upper mass limit for the companions around our stars using the Baraffe et al. (2015) evolutionary models, finding the closest point matching the spectral temperature cut-off and logg = 5.0. These values are given in Table 6 and are between 560 and 618 M_{Jup}. The flux ratio between
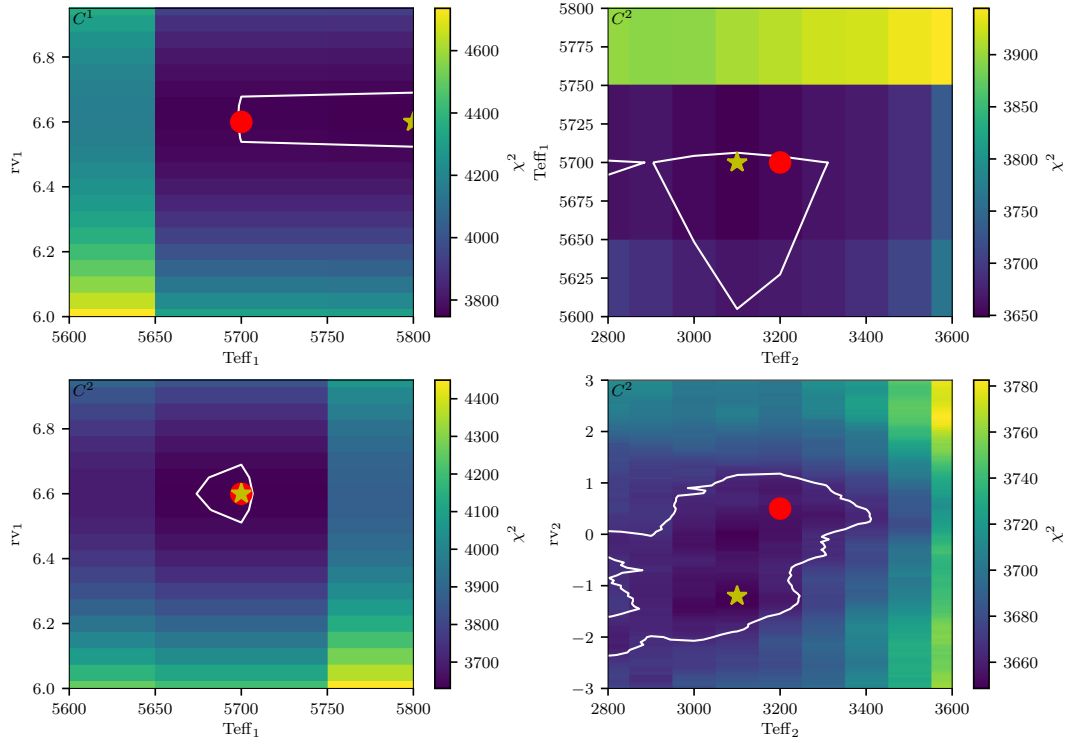
Figure 5. χ^2 result grid for observation 2 of HD 211847, similar to Figs. 3 and 4. The top right plot shows the application of a single component model (C^1) while the other three are using a binary model (C^2). Both left hand panels show the distribution of host temperature and host RV. The top right panel shows the distribution for host and companion temperature, and the bottom right the companion temperature and radial velocity. The red circles indicate the literature values or calculated parameters for the target while the yellow star indicates the minimum χ^2 solution. The error bar on T_{eff_1} is from the literature while the error bars on rv_1 and rv_2 are calculated by propagating the orbital parameter uncertainties though the radial velocity equation. The white line shows a 3-σ confidence level about the minimum χ^2 solution grid point, not always visible here due to the large χ^2 values.

the cut-off and the host star are also provided for, being between 5 and 15 per cent in this wavelength span.

It is important to note that the objective of this exercise was not as much to reproduce exactly the detection with real spectra but to provide a ground for comparison.

6 DISCUSSION

The synthetic recovery method attempted here was unsuccessful in the detection of the BD companion spectra. The upper mass limits of 600^{+20}_{-40} M_{Jup} we set for these companions is very high, roughly six times higher then the BD mass limit ~80–90 M_{Jup}. We discuss potential reasons and solutions for these poor results below, list the lessons learned in this exploratory study of this dataset, and provide some guidance for any future attempts with these methods.

6.1 Synthetic recovery limitations

6.1.1 Mismatch in synthetic models

We believe the spectral mismatch between the observation and synthetic spectra is the main cause for the unsuccessful companion detection with the χ^2 method. The absence in the observed spectra of strong lines predicted by the model impacts the recovery in two ways; the spectral mismatch increases the χ^2 values and pushes the companion temperature to higher temperatures, up to the constraints allowed by the grid.

In our examples the logg and metallicity of the synthetic models are held fixed, leaving only temperature to vary. Changing the temperature affects the synthetic spectral models in two main ways: the flux level of the continuum, and the number and strength of the absorption lines. In the binary model the contributions from the individual components is scaled by the flux ratio. If the temperature of the companion increases then the flux and radius of the companion increases. The contribution of the companion to the binary model increases and the flux ratio F_1/F_2 decreases. This effectively makes the lines of the spectrum of the host component relatively smaller in the normalized binary model spectrum. Due to the large initial mismatch of synthetic spectral lines of the host, a decrease in relative strength of the host lines decreases the χ^2 value, and provides a better "match" to the observation. This effect increases artificially the temperature of the recovered companion. If the companion temperature grid is allowed to extend, it will recover a companion with a temperature >2000 K above the expected temperature. The χ^2 approach is thus actually dominated by reducing the mismatch in the spectrum of the host rather than actually detecting the spectra of the companion. When preforming the simulations in Sect. 5.1 there is no spectral mismatch between the simulation and the models, and as such we recover the correct host spectra and recover parameters for the companion much closer to the injected.

To specifically check that the mismatch was not due to errors in our reduction we obtained the final spectral atlas of 10 LEO from the CRIRES-POP archive, fully reduced and telluric corrected (Nicholls et al. 2017). Comparing the spectrum of 10 LEO to a PHOENIX-ACES model with the corresponding parameters T_{eff_1} = 4800 K,
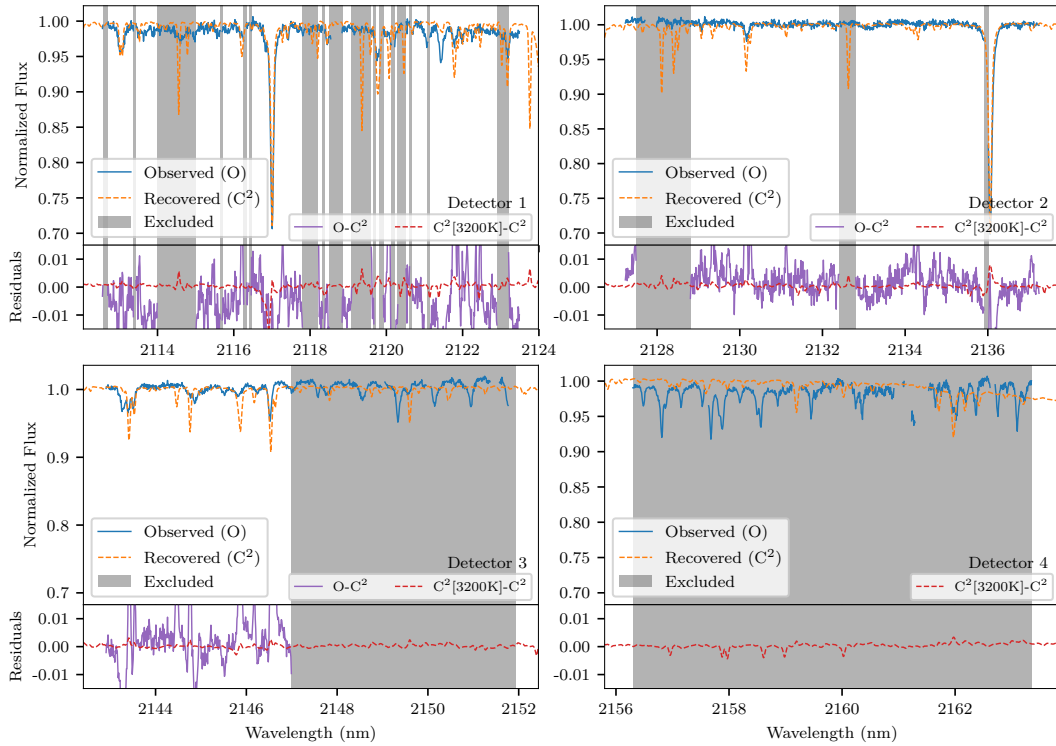
Figure 6. Comparison between the observed HD 211847 spectrum (blue) and the best fit synthetic binary model (orange dashed) for each detector. The bottom section of each panel shows the residuals between the parts of the observation used in the χ^2 fit and recovered binary model $(O - C^2)$ in purple. The red dashed line shows the difference between the recovered binary model and the binary model with the exact same parameters except for the estimated companion temperature of 3200 K $(C^2[3200K] - C^2)$. The grey shading indicated the wavelength regions where masking has been applied. The thinner masked regions that match with cuts in the observed spectra are where the centres of deep (>5 per cent) telluric lines that have been masked out are.
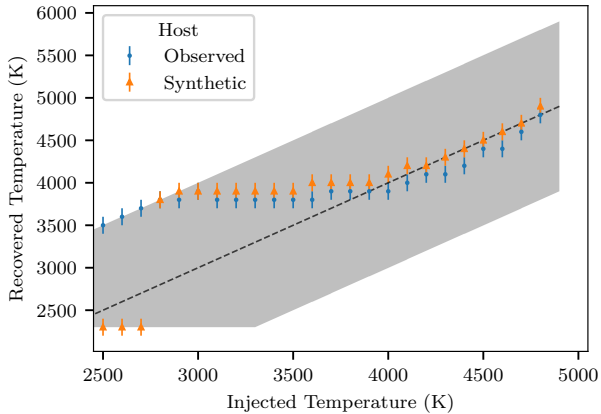
Figure 7. Result of simulated injection-recovery of synthetic companions on HD 30501. The blue dots and orange triangles indicate the recovered companion temperature for the observed and synthetic spectra respectively. The ±100 K error bars are the grid step of the synthetic models. The black dashed diagonal shows the 1:1 temperature relation. The grey shaded region indicates the ±1000 K temperature range explored. Gaussian noise added to the synthetic spectra was derived from the observed spectra.

logg=3.0, [Fe/H] = 0.0 and convolved to R=90 000, similar line mismatches are observed. For 10 LEO, the match to the model is better than in our case, but in the region of our observations between 2110–2160 nm there are deep lines in the model that are not observed, lines that have significantly different strengths, lines observed that are not modelled whilst other lines 'appear' to be

offset in wavelength, at the same positions as observed in the work presented here. This indicates that the mismatch is not specific to our reduction only and that there is still room for improvement in synthetic models around 2100 nm. Other works have also indicated regions or specific lines in which synthetic models did not reproduce all of the spectral features seen in stellar spectra (e.g. Del Burgo et al. 2009; Bonnefoy et al. 2014; Passegger et al. 2016a; Rajpurohit et al. 2016).

6.1.2 Line contribution of faint companions

We calculate the line depths of the synthetic companion spectra to determine the SNR levels required to detect the lines of the binary companions. One thing easy to overlook when attempting to detect the binary companion at low flux ratios is the actual contribution of the spectral lines of the companion. The flux ratio of the continuum for our most promising target is $F_2/F_1 \sim 1$ per cent with the other targets having an expected flux ratio 0.5 per cent, and some well below. At wavelengths between 2110–2160 nm, the spectral lines of the individual components have depths on average around 10–20 per cent of their respective continua; as such the companion line features have a depth $\ll 1$ per cent relative to the continuum of the combined spectra.

In Table 7 we calculate some properties of the spectral lines in the PHOENIX-ACES library between 2110–2160 nm. We count the number of spectral lines (*no. lines*) deeper than 5 per cent, and take the average depth (*avg. depth*) of these lines. The contribution *comp. depth* of the companion lines to a combined spectrum accounts for the flux ratio between the two components. Here we use a Sun-like
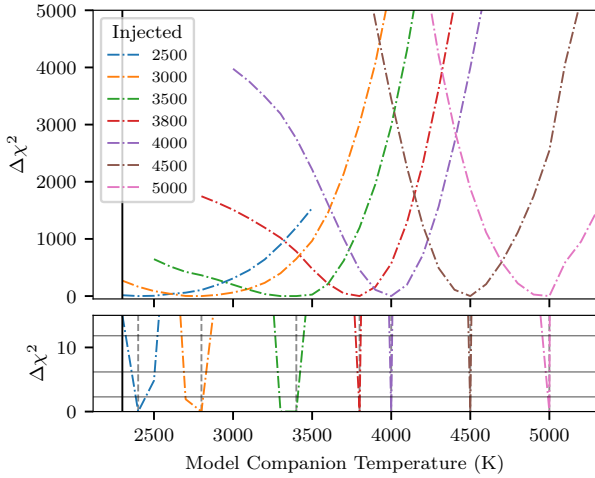
Figure 8. (top) Companion temperature verses χ^2 for simulations with different injected companion temperatures. Other fixed parameters for these fully synthetic simulations was T_{eff_1} = 5200 K, logg_1 = 4.5, logg_2 = 5.0, and both [Fe/H] = 0.0. A fixed Gaussian noise corresponding to a SNR of 300 was used. (bottom) A close up view of χ^2 < 15. The three horizontal grey lines indicate the 1, 2, 3 sigma with 2 degrees of freedom. The vertical dotted lines indicate the location of the minimum χ^2 recovered for each companion. The black solid vertical in both panels shows the 2300 K cut-off of the PHOENIX-ACES models

host with T_{eff_1} = 5800 K. This simplified combination neglects the continuum shapes of both spectral components and uses the average flux ratios for this wavelength range. The PHOENIX-ACES spectra in the temperature range of 2500–5000 K shown in Fig. 9 can be used to get a visual indication of the line density and depth measured here.

There are more lines >5 per cent deep for the lower temperature spectra, with 360–460 lines in this wavelength range, to be compared with the 31 deep absorption lines found in a Sun-like spectrum. The average line depth of these lines is also larger than the Sun-like spectrum, around twice as deep. However, when combined, the contribution of the companion lines is 1–2 orders of magnitude smaller than the hosts lines due to the low continuum flux ratios.

For example, with the synthetic model for the companion of HD 211847, the average contributions of lines >5 per cent become only 0.3 per cent deep in a binary with the Sun-like spectrum. For a companion with a temperature of 2300 K (the lower PHOENIX-ACES temperature limit) the deepest lines contribute lines around 0.1 per cent.

The SNR of the observed spectra is between 150–350, which is below the SNR of 323 needed for the detection of the low-mass star companion of HD 211847 with temperature 3200 K and logg 5.0. For our other targets with BD companions at and below the PHOENIX-ACES temperature range, we would need observed SNR >800 to detect the individual spectral lines of the companion. With the SNR increasing with $\sqrt{N}$ this would require the observational time for each target to be increased by a factor of ∼10–64. This is in line with the recent detection of the spectrum of a non-transiting giant planet by Piskorz et al. (2016) which utilized nIR spectra with SNR > 2000, from 1–3 hours of observation each.

Our non-detection of binary companions with low flux ratios is consistent with results from other works. For example Nemravová et al. (2016) performed extensive spectral analysis of a quadruple-star system ξ Tauri using 227 spectra in 3 different wavelength bands. Of the four stars in the system, the authors were unable to

Table 7. Contribution of synthetic lines within 2110–2160 nm of synthetic PHOENIX-ACES spectra to a binary model. F_2/F_1 is the continuum flux ratio between a spectrum with the given T_{eff} and logg and a Sun-like spectrum with T_{eff} = 5800, logg = 4.5 (right most column). *No. lines* is the number of spectral lines deeper than 5 per cent from the continuum of the individual spectra while *avg. depth* is the mean depth of those lines. *Comp. depth* is the average contribution, or depth, of these companion lines in a binary with a Sun-like star. The SNR is the signal-to-noise level required to have achieve a Gaussian noise σ = 1/SNR level equal to the *comp. depth* level in the binary model. All synthetic spectra used here have [Fe/H] = 0.0.

T_{eff} (K)	2300		3200		5800 (F_1)
logg	5.0	4.5	5.0	4.5	4.5
F_2/F_1	0.006	0.019	0.029	0.091	1.000
no. lines	464	463	365	413	31
avg. depth	0.2	0.23	0.11	0.12	0.10
comp. depth[a]	0.0012	0.0043	0.0031	0.0100	0.0833[b]
SNR	833	232	323	100	12

[a] avg. depth $\times$ $F_2/(F_1 + F_2)$, where F_1 is the component in the far right column.   [b] avg. depth $\times$ $F_1/(F_1 + F_2)$, where F_2 is for the companion with T_{eff} = 3200, logg = 4.5.

detect the spectral component of the one with a luminosity ratio below 1 per cent. The secondary detection in optical spectra using spectral matching of KOI was also only able to reach flux ratios of 1 per cent Kolbl et al. (2015).

6.1.3 χ^2 asymmetry

In Fig. 8 we show that the shape of the recovered χ^2 becomes asymmetric when dealing with companion temperatures below around 3800 K. A visual inspection of the spectra reveals the likely cause. In Fig. 9 we show the corresponding spectra between 2111–2165 nm. As the temperature decreases the strongest lines become less prominent, disappearing progressively among the other many small lines that appear at lower temperatures. Hence there are no strong companion lines to easily distinguish one temperature from another. In the flatter part of the χ^2 curves several low temperature companions are equally well fitted to the simulation/observation.

Figures 7 and 8 show different recovered temperatures but both agree above 3800 K. A higher companion temperature is recovered between 2800 and 3800 K, whereas in Fig. 8 a lower temperature is recovered. This is probably due to a combination of the noise added, and the asymmetries of the χ^2 lines. Figure 7 uses the noise level from the observed spectrum while Fig. 8 has a SNR of 300. This large asymmetry can also explain the jump observed in the synthetic recovery temperature around 2700 K in Fig. 7.

The asymmetry also causes an asymmetry in the χ^2 error bars which can be seen in the bottom panel of Fig. 8. For instance the recovered value and 1-σ error bars on the 3000 K injected companion is 2800^{+20}_{-100}, with an asymmetric error bar skewed towards lower temperatures.

The bump observed at 5100 K in the χ^2 curves is due to a discontinuity in the PHOENIX-ACES modelling. The "reference wavelength defining the mean optical depth grid" is changed at 5000 K (Husser et al. 2013, Sect. 2.3). Care needs to be taken if trying to detect a companion near this temperature.

6.1.4   Component RV separation

Another factor that can contribute to an unsuccessful detection is the RV separation between the host and companion, rv_2. Estimates
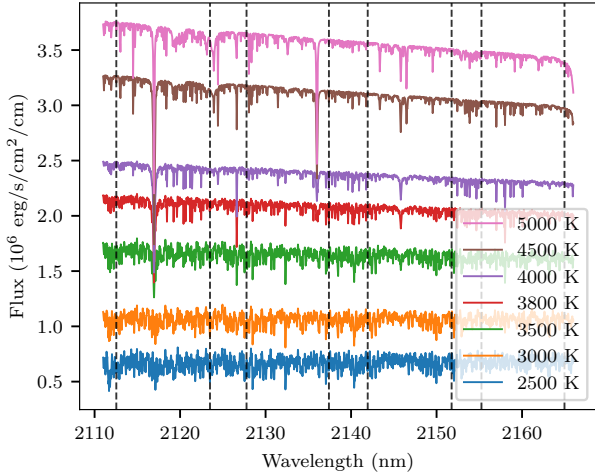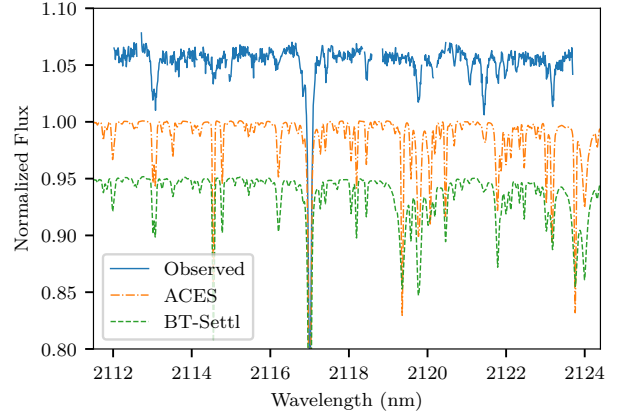
Figure 9. PHOENIX-ACES spectra for temperatures between 2500 and 5000 K, corresponding to to the same lines in Fig. 8. The flux units are the native units of the PHOENIX-ACES spectrum, (erg s^{-1} cm^2 cm^{-1}), and have not been scaled by the stellar radii. All spectra have a logg = 5.0 and [Fe/H] = 0.0. The vertical dotted lines indicate the edges of the CRIRES detectors.

Figure 10. Detector 1 spectrum for HD 211847 (blue) alongside the PHOENIX-ACES (orange dash-dot) and BT-Settl (green dashed) synthetic spectra for the host star only, with parameters $T_{\rm eff}$ = 5700 K, logg = 4.5 and [Fe/H] = 0.0. Both synthetic models have been normalized and convolved to R = 50 000. There is a 0.05 off-set between each spectrum

for our observations are given in the last column of Table 3. If rv_2 is small compared to the line width, then all the same lines of both components will be blended. This is indeed the case for the observations of HD 4747, HD 211847, and HD 202206 with expected $|rv_2| < 2\,{\rm km s}^{-1}$, which were affected poor observational planning. This may have contributed to the lack of recovery of the two components of the binary model. Having multiple spectra of the same target distributed in phase may allow the RV of the spectral components to be better recovered (e.g. Czekala et al. 2017; Sablowski & Weber 2016). In a similar way, Kolbl et al. (2015) were unable to detect companion stars within $10\,{\rm km s}^{-1}$ of the host using optical spectra.

6.1.5 Wavelength range

The wavelength range for these observations was chosen specifically due to the location of the *K*-band telluric absorption window. This was to reduce telluric contamination present in the spectra intended for the spectral differential technique. The wavelength range is also very narrow (~50 nm), an aspect set by the CRIRES instrument specifications. The small number and inconsistent distribution of telluric lines made the wavelength calibration method using the telluric lines difficult in some regions (specifically detectors 2 and 3). For the χ^2 fitting of faint companions this narrow wavelength region is likely not the best choice given the small number of stellar lines and unique spectral features of the companion. For example Passegger et al. (2016b) use 4 different wavelength regions with lines from different species to fit PHOENIX-ACES models to M-dwarf stars while other studies aiming to detect planetary companions choose wavelength regions which contain strong planetary absorption features such as the absorption of CO and H_2O near 2.3 μm (e.g. de Kok et al. 2013; Brogi et al. 2014). Applying the binary fitting to a different wavelength region with lines more sensitive to stellar parameters for both stars and BDs, as well as using a larger wavelength range (i.e. provided by the cross-dispersion on CRIRES+ (Dorn et al. 2016)), should improve the recovery results of the technique presented here. We note that if the wavelength range is increased by

taking separate observations at different wavelengths, not covered by a single exposure, then changes in the RV of both components between the different wavelength observations will need to be accounted for.

6.1.6 The BT-Settl models

The PHOENIX-ACES models are not the only spectral libraries available, with the other notable library considered for this work being the BT-Settl models (Allard et al. 2010; Allard 2013; Baraffe et al. 2015). These modelling of dust and cloud formation, as well as hydro-dynamical modelling atmospheric mixing/settling for atmospheres with $T_{\rm eff}$ below ~2600 K, make the BT-Settl models valid across the regime from stars to BDs as cool as 400 K. As the BT-Settl models are suitable to model the atmospheres of the brown dwarfs they would be useful for the companion recovery technique developed here. However, as shown in Sect. 5.2 and 5.3, we were unable to successfully recover the 155 M_J ($T_{\rm eff}$ ~3200 K) low mass star companion of HD 211847 and derived a temperature upper limit for our methodology of around 3800 K. These are both well above the 2300 K cut-off of the PHOENIX-ACES models and for the onset of dust- and cloud-formation phenomena, at 2600 K.

Fig. 10 shows again the minimum χ^2 solution for detector 1 of the second HD 211847 observation, this time including the BT-Settl solution with the same parameters. Although the PHOENIX-ACES and BT-Settl models differ slightly they both have a large spectral mismatch to the observations. As such, the conclusions reached above on PHOENIX-ACES models are also extendable to BT-SETTL

Although the newer generations synthetic spectral models are improving and match the overall spectral energy distribution reasonably well, there are still regions in the *H*- and *K*-band where there is room for improvement Rajpurohit et al. (2016). The spectral mismatch in the region studied here is still too large for an accurate spectral recovery of companion brown dwarfs. By observing in the nIR we have a compound problem: a poorer model matching at sub-stellar temperatures, with poorer chemistry characterization combined with the accrued difficulties of observing in the nIR (e.g. telluric absorption, higher background, poorer detectors.).

6.1.7 Impact of logg

Logg, a measure of surface gravity, is related to evolutionary state and the size of the star with smaller logg values usually indicating larger radii stars. This parameter has a large impact on the radius and flux ratio of the binary models. In the PHOENIX-ACES models a decrease in logg from 5.0 to 4.5 increases the models effective radius by ~1.75 in the temperature range investigated here. This change in radius alone roughly triples (1.75^2) the absolute flux of the synthetic spectrum, neglecting any changes to the shape of the actual spectrum. Therefore, there are large jumps in the model flux ratios if the logg is allowed to vary, with lower logg values for the companion being favoured as the increased flux ratio decreases the mismatch of the host component to the observations. This large impact of logg on the spectral library absolute flux is one reason for keeping the logg of each component fixed in the χ^2 results presented in Sect. 5.

6.1.8 Interpolation

It is common to interpolate between the synthetic spectral grids to fit and derive parameters in between the grid points (e.g. Nemravová et al. 2016; Passegger et al. 2016b). Instead of interpolation Czekala et al. (2015) use a spectral emulator to use Principal Component Analysis to create eigenspectra for the synthetic library and Gaussian processes to derive a probability distribution function of possible interpolation spectra to account for uncertainties in the interpolation required for high signal-to-noise spectra.

However, we did not incorporate any interpolation into the companion recovery at this stage. This could be something to be added in the future to refine the recovered parameters, and to help the transition between the grid logg values. Codes are readily available to perform spectral interpolation which could be utilized for this, two of them are PYTERPOL[11] Nemravová et al. (2016) and STARFISH[12] (Czekala et al. 2015).

6.2 Future implementation

6.2.1 High resolution instrumentation

The future of high resolution near- and mid- IR spectrographs is looking bright, with many new ground- and space-based instruments currently being developed. Notable examples include CARMENES (550–1710 nm, R=82 000) which is now operational (Quirrenbach et al. 2014), while SPIRou (980–2350 nm, R=73 500) (Artigau et al. 2014) and NIRPS (970–1810 nm, R=100 000) (Bouchy et al. 2017) are still being assembled and installed. The eagerly awaited *JWST* (Gardner et al. 2006) will provide observations in both the near-IR (600–5300 nm, R=2700) and mid-IR (4900–28 800 nm, R~1550–3250) regions without contamination from our atmosphere.

The upgrade of CRIRES to CRIRES+ (Dorn et al. 2016) will increase the wavelength coverage of a single shot capture by at least a factor of 3–5. This larger wavelength span will be extremely beneficial for the χ^2 performance of the spectral recovery method, increasing the number of useful lines and spectral features to be fitted with the models.

On the modelling side, there are continual improvements in

atmospheric modelling and their associated synthetic spectral libraries: as seen with the evolution of the BT-Settl models (Allard 2013). With additional physics and improved line lists and solar abundances (e.g. Asplund et al. 2009; Caffau et al. 2011), the synthetic libraries are reaching a better agreement with nIR observations. An improved agreement between the nIR observations and synthetic spectra will be crucial to improve the performance of the spectral recovery technique presented here.

Although not successful with the CRIRES data used here, the instrumental stage is set to attempt these techniques presented here using the next-generation of high resolution spectrographs. The lessons learned in this analysis need to be taken into account in order to achieve the best chance of a successful detection.

6.3 Other techniques

We note that there are many other disentangling techniques to separate mixed spectra of binary systems, (e.g. Hadrava 2009). These require more than two observations, with $n + 1$ observations used to set up a system of linear equations to solve for n spectral components (e.g. Simon & Sturm 1994; Czekala et al. 2017; Sablowski & Weber 2016). These methods are ideal for many well spaced observations. For example the ideal situation for the SVD method of Sablowski & Weber (2016) is homogeneous samples of at least half the period, to identify the moving spectral components. Recently, the cross-correlation and maximum-likelihood techniques (e.g. Lockwood et al. 2014; Piskorz et al. 2016) have been successful in detecting the faint companion spectra of giant planets using several spectra with very-high SNR (>2000) obtained with longer observational time (1–3 hours) each taken across the full orbital range. The few, short and insufficiently separated observations we analyse here are not suitable to apply these advanced techniques and are beyond what we have attempted here.

The recent work of Piskorz et al. (2016) use a PCA technique to correct for the telluric spectra by applying it to several AB nodding pairs over their 60–180 minute integration time. We are uncertain if this technique would work as effectively on our observations due to our shorter integration time (24 minutes) would have less telluric variation present across the 8 nod spectra. A recent comparison of three telluric correction methods, MOLECFIT and TELFIT and TAPAS to the standard star method by (Ulmer-Moll et al. 2018) found that all three synthetic models preform better at correcting for atmospheric H_2O compared to the standard star method with MOLECFIT, being a more complete tool, preforming slightly better over TAPAS.

7 CONCLUSIONS

This work explored a spectral recovery technique to detect the faint spectra of stellar companions in a composite spectra, using high resolution near-infrared spectra.

This work highlights many of the difficulties when dealing with the spectral recovery of nIR spectra. The obstacles to overcome are the data reduction of nIR CMOS detectors, that are not yet at the level of visible CCDs, along with a precise telluric correction and wavelength calibration (two interrelated aspects, as thoroughly discussed). Another important aspect is the mismatch between nIR high-resolution spectra and the observed spectra. In spite of the continuous effort of the modelling community, our work, along with several cited contemporary ones, shows that this mismatch is still one of the main factors preventing us from performing spectral recovery in the nIR. This work highlights that this is a compound

---

[11] https://github.com/chrysante87/pyterpol
[12] https://github.com/iancze/Starfish

problem for Brown Dwarfs, for which the spectral models are worse informed due to lack of observations at high-resolution.

Other than the improvement of the spectral models, the observing community can increase their odds of success by paying attention to the scheduling of observations and the wavelength domains to explore. Our work shows that observing in the areas of lower telluric absorption, as is frequently done, is not a guarantee of success due to the scarcity of deep lines in cold objects. Moreover, due to the mismatch between models and observations, the ability to obtain a first spectra before settling on a wavelength range, or changing settings on the fly, is extremely useful for the success of these campaigns.

We hope that this work can act as a guide for the planning of future observations of targets with faint BD and planetary companions with the upcoming generation of high resolution spectrographs in the near- and mid-infrared such as CRIRES+ and JWST observations.

REFERENCES

Adibekyan V. Z., Sousa S. G., Santos N. C., Mena E. D., Hernández J. I. G., Israelian G., Mayor M., Khachatryan G., 2012, Astronomy and Astrophysics, 545, A32

Allard F., 2013, Proceedings of the International Astronomical Union, 8, 271

Allard F., Homeier D., Freytag B., 2010, arXiv:1011.5405 [astro-ph]

Artigau E., et al., 2014, in Proc.SPIE. International Society for Optics and Photonics, p. 914715, doi:10.1117/12.2055663

Asplund M., Grevesse N., Sauval A. J., Scott P., 2009, Annual Review of Astronomy and Astrophysics, 47, 481

Astudillo-Defru N., et al., 2015, Astronomy and Astrophysics, 575, A119

Baraffe I., Chabrier G., Barman T., Allard F., Hauschildt P. H., 2003, Astronomy and Astrophysics, 402, 701

Baraffe I., Homeier D., Allard F., Chabrier G., 2015, Astronomy and Astrophysics, 577, A42

Barnes J. R., Barman T. S., Jones H. R. A., Leigh C. J., Cameron A. C., Barber R. J., Pinfield D. J., 2008, Monthly Notices of the Royal Astronomical Society, 390, 1258

Bean J. L., Miller-Ricci Kempton E., Homeier D., 2010, Nature, 468, 669

Benedict G. F., Harrison T. E., 2017, The Astronomical Journal, 153, 258

Bertaux J. L., Lallement R., Ferron S., Boonne C., Bodichon R., 2014, Astronomy and Astrophysics, 564, A46

Bevington P. R., Robinson D. K., 2003, Data Reduction and Error Analysis for the Physical Sciences. McGraw-Hill

Birkby J. L., de Kok R. J., Brogi M., Schwarz H., Snellen I. A. G., 2017, The Astronomical Journal, 153, 138

Bonfanti A., Ortolani S., Nascimbeni V., 2016, Astronomy and Astrophysics, 585, A5

Bonnefoy M., Chauvin G., Lagrange A.-M., Rojo P., Allard F., Pinte C., Dumas C., Homeier D., 2014, Astronomy and Astrophysics, 562, A127

Bouchy F., et al., 2017, The Messenger, 169, 21

Brogi M., Snellen I. A. G., de Kok R. J., Albrecht S., Birkby J., de Mooij E. J. W., 2012, Nature, 486, 502

Brogi M., de Kok R. J., Birkby J. L., Schwarz H., Snellen I. A. G., 2014, Astronomy and Astrophysics, 565, A124

Brogi M., de Kok R. J., Albrecht S., Snellen I. A. G., Birkby J. L., Schwarz H., 2016, The Astrophysical Journal, 817, 106

Burrows A., et al., 1997, The Astrophysical Journal, 491, 856

Caffau E., Ludwig H.-G., Steffen M., Freytag B., Bonifacio P., 2011, Solar Physics, 268, 255

Chabrier G., Baraffe I., 2000, Annual Review of Astronomy and Astrophysics, 38, 337

Clough S. A., Iacono M. J., 1995, Journal of Geophysical Research: Atmospheres, 100, 16519

Correia A. C. M., Udry S., Mayor M., Laskar J., Naef D., Pepe F., Queloz D., Santos N. C., 2005, aap, 440, 751

Cotton D. V., Bailey J., Kedziora-Chudczer L., 2014, Monthly Notices of the Royal Astronomical Society, 439, 387

Crepp J. R., Gonzales E. J., Bechter E. B., Montet B. T., Johnson J. A., Piskorz D., Howard A. W., Isaacson H., 2016, The Astrophysical Journal, 831

Czekala I., Andrews S. M., Mandel K. S., Hogg D. W., Green G. M., 2015, The Astrophysical Journal, 812, 128

Czekala I., Mandel K. S., Andrews S. M., Dittmann J. A., Ghosh S. K., Montet B. T., Newton E. R., 2017, The Astrophysical Journal, 840, 49

Czesla S., Molle T., Schmitt J. H. M. M., 2018, Astronomy and Astrophysics, 609, A39

Deeg H., 1998, in Brown Dwarfs and Extrasolar Planets. p. 216

Del Burgo C., Martín E. L., Zapatero Osorio M. R., Hauschildt P. H., 2009, Astronomy and Astrophysics, 501, 1059

Dorn R. J., et al., 2016, in Ground-Based and Airborne Instrumentation for Astronomy VI. International Society for Optics and Photonics, p. 99080I

Ferluga S., Floreano L., Bravar U., Bédalo C., 1997, Astronomy and Astrophysics Supplement Series, 121, 201

Figueira P., et al., 2010, Astronomy and Astrophysics, 511, A55

Figueira P., et al., 2016, Astronomy and Astrophysics, 586, A101

Gardner J. P., et al., 2006, Space Science Reviews, 123, 485

Gullikson K., Dodson-Robinson S., Kraus A., 2014, The Astronomical Journal, 148, 53

Hadrava P., 2009, arXiv:0909.0172 [astro-ph]

Halbwachs J.-L., Arenou F., Mayor M., Udry S., Queloz D., 2000, Astronomy and Astrophysics, 355, 581

Hatzes A. P., Rauer H., 2015, The Astrophysical Journal Letters, 810, L25

Horne K., 1986, Publications of the Astronomical Society of the Pacific, 98, 609

Husser T.-O., von Berg S. W., Dreizler S., Homeier D., Reiners A., Barman T., Hauschildt P. H., 2013, Astronomy and Astrophysics, 553, A6

Kaeufl H.-U., et al., 2004, Ground-based Instrumentation for Astronomy, 5492, 1218

Kerber F., Nave G., Sansonetti C. J., Bristow P., 2009, Physica Scripta, 2009, 014007

Kolbl R., Marcy G. W., Isaacson H., Howard A. W., 2015, The Astronomical Journal, 149, 18

Kostogryz N., Kürster M., Yakobchuk T., Lyubchik Y., Kuznetsov M., 2013, Astronomische Nachrichten, 334, 648

---

[13] Available at https://pyastronomy.readthedocs.io

Lockwood A. C., Johnson J. A., Bender C. F., Carr J. S., Barman T., Richert A. J. W., Blake G. A., 2014, The Astrophysical Journal Letters, 783, L29

Maldonado J., Villaver E., 2017, Astronomy and Astrophysics, 602, A38

Moutou C., Vigan A., Mesa D., Desidera S., Thébault P., Zurlo A., Salter G., 2017, Astronomy and Astrophysics, 602, A87

Nemravová J. A., et al., 2016, Astronomy and Astrophysics, 594, A55

Nicholls C. P., et al., 2017, Astronomy and Astrophysics, 598, A79

Passegger V. M., et al., 2016a, arXiv:1607.08738 [astro-ph 10/gdwsfp

Passegger V. M., Berg S. W.-v., Reiners A., 2016b, Astronomy and Astrophysics, 587, A19

Pilyavsky G., et al., 2011, apj, 743, 162

Piskorz D., et al., 2016, The Astrophysical Journal, 832, 131

Piskunov N. E., Valenti J. A., 2002, Astronomy and Astrophysics, 385, 1095

Quirrenbach A., et al., 2014, in Prococeedings of SPIE: Ground-Based and Airborne Instrumentation for Astronomy V. p. 91471F, doi:10.1117/12.2056453

Rajpurohit A. S., Reylé C., Allard F., Homeier D., Bayo A., Mousis O., Rajpurohit S., Fernández-Trincado J. G., 2016, Astronomy and Astrophysics, 596, A33

Rodler F., Lopez-Morales M., Ribas I., 2012, The Astrophysical Journal Letters, 753, L25

Rothman L., et al., 2009, Journal of Quantitative Spectroscopy and Radiative Transfer, 110, 533

Rothman L., et al., 2013, Journal of Quantitative Spectroscopy and Radiative Transfer, 130, 4

Sablowski D. P., Weber M., 2016, Astronomy and Astrophysics

Sahlmann J., et al., 2011, Astronomy and Astrophysics, 525, A95

Santerne A., et al., 2012, Astronomy and Astrophysics, 545, A76

Santos N. C., Israelian G., Mayor M., 2004, Astronomy and Astrophysics, 415, 1153

Santos N. C., Israelian G., Mayor M., Bento J. P., Almeida P. C., Sousa S. G., Ecuvillon A., 2005, aap, 437, 1127

Santos N. C., et al., 2017, Astronomy and Astrophysics, 603, A30

Schlaufman K. C., 2018, The Astrophysical Journal, 853, 37

Schwarz G., 1978, The Annals of Statistics, 6, 461

Seifahrt A., Käufl H. U., Zängl G., Bean J. L., Richter M. J., Siebenmorgen R., 2010, Astronomy and Astrophysics, 524, A11

Simon K. P., Sturm E., 1994, Astronomy and Astrophysics, 281, 286

Smette A., et al., 2015, Astronomy and Astrophysics, 576, A77

Snellen I. A. G., de Kok R. J., De Mooij E. J. W., 2010, Nature, 465, 1049

Snellen I. A. G., Brandl B. R., De Kok R. J., Brogi M., Birkby J., Schwarz H., 2014, Nature, 509, 63

Soderblom D. R., 2010, Annual Review of Astronomy and Astrophysics, 48, 581

Sorahana S., Yamamura I., Murakami H., 2013, The Astrophysical Journal, 767, 77

Sousa S. G., et al., 2008, aap, 487, 373

Tody D., 1993, in Hanisch R. J., Brissenden R. J. V., Barnes J., eds, Astronomical Society of the Pacific Conference Series Vol. 52, Astronomical Data Analysis Software and Systems II. p. 173

Tsantaki M., Sousa S. G., Adibekyan V. Z., Santos N. C., Mortier A., Israelian G., 2013, aap, 555, A150

Udry S., Mayor M., Naef D., Pepe F., Queloz D., Santos N. C., Burnet M., 2002, Astronomy and Astrophysics, 390, 267

Ulmer-Moll S., Figueira P., Neal J. J., Santos N. C., Bonnefoy M., 2018, arXiv e-prints, p. arXiv:1811.08915

Vacca W. D., Cushing M. C., Rayner J. T., 2003, Publications of the Astronomical Society of the Pacific, 115, 389

Wenger M., et al., 2000, Astronomy and Astrophysics Supplement Series, 143, 9

Whitworth A., Bate M. R., Nordlund A., Reipurth B., Zinnecker H., 2007, Protostars and Planets V, pp 459–476

Zechmeister M., et al., 2018, Astronomy and Astrophysics, 609, A12

Zucker S., Mazeh T., 2001, The Astrophysical Journal, 562, 549

de Kok R. J., Brogi M., Snellen I. A. G., Birkby J., Albrecht S., de Mooij E. J., 2013, Astronomy and Astrophysics, 554, A82

APPENDIX A: ESTIMATING COMPANION PARAMETERS

In Table A1 we present the flux ratio for the sudied systems based on their published masses M_2 or $M_2 \sin i$ and K_2 for each companion. We refer to these calculations as estimates as in some cases we only have the companions minimum mass.

The host companion contrast ratio is calculated from the magnitude difference. Magnitudes for the companion are interpolated from the Barraffe tables.

A simple tool[14] was created to calculate the flux ratio using the (Baraffe et al. 2003, 2015) evolution tables. Given the host star name, the companion mass and a stellar age it interpolates the available Baraffe tables to the companion mass and age specified. The host's name is used to query the SIMBAD database to obtain stellar properties, specifically magnitudes, to calculate the flux ratios. It can also work in reverse to estimate a companion mass when provided with a flux ratio.

This paper has been typeset from a TeX/LaTeX file prepared by the author.

---

[14]   Available at https://github.com/jason-neal/baraffe_tables

Table A1. Estimated flux ratios, orbital semi-amplitude and RV separation of the companion, given the companion mass (M_2 or $M_2 \sin i$) from Table 2 and observation times from Table 3.

Companion	Host M_K (mag)	Companion M_K (mag)	Estimated F_2/F_1 K-band	Estimated N_2/N_1 (noise ratio)	Estimated K_2 ($km s^{-1}$)	Estimated ΔRV ($m s^{-1}$)	Phase coverage (%)
HD 4747	3.82	14.17	7×10^{-5}	76	-10.65	–	–
HD 162020	4.10	23.36	2×10^{-8}	1615	-98.92[a]	2344.24	0.28
HD 167665	2.60	13.21	6×10^{-5}	105	-14.47[a]	138.45	0.18
HD 168443b	2.35	42.19	1×10^{-16}	1×10^8	-64.65[a]	257.16	0.035
HD 168443c	2.35	29.55	1×10^{-11}	4×10^5	-18.05[a]	0.95	0.001
HD 202206B	3.04	21.63	4×10^{-8}	1586	-6.79	145.17	0.74
HD 202206c	3.04	45.63	9×10^{-18}	2×10^7	-2.50	0.67	0.15
HD 211847B	3.50	8.40	0.011	14	-1.85	3.88	0.09
HD 30501	3.96	10.38	0.003	27	-16.12	1346.46	5.8

[a] Maximum K_2 only given $M_2 \sin i$